December 1995

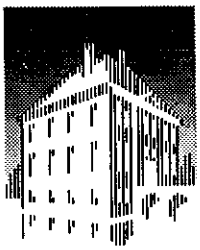

FOM-Instituut voor Plasmafysica Rijnhuizen Associatie Euratom-FOM

Postbus 1207
3430 BE Nieuwegein
Nederland
Edisonbaan 14
3439 MN Nieuwegein
Tel. + 31(0)30-6096999
Fax. + 31(0)30-6031204

MHD STABILITY ANALYSIS of the KT-2 tokamak plasma

S. POEDTS, A. DE PLOEY*, and J.P. GOEDBLOED

* Permanent address: Centre for Plasma Astrophysics, K.U. Leuven, Celestijnenlaan 200B, 3001 Heverlee, Belgium.

This work was performed as part of the research programme of the association agreement of Euratom and the 'Stichting voor Fundamenteel Onderzoek der Materie' (FOM) with financial support from the 'Nederlandse Organisatie voor Wetenschappelijk Onderzoek' (NWO), Euratom, and by the Korean Atomic Energy Research Institute (KAERI)

RIJNHUIZEN
REPORT
96-227

Contents

1 Introduction

This is the final report on the project 'MHD stability analysis of the KT-2 tokamak plasma'. The stability of toroidal axisymmetric divertor tokamak plasmas with up-down symmetric plasma cross-sections and KT-2 relevant plasma and device parameters has been investigated in the framework of ideal and dissipative linearized magnetohydrodynamics (MHD).

In the next Section, some equilibrium features that are frequently used in this report are briefly reviewed and notation agreements are made. Also, the applied definitions of some basic plasma parameters are given in order to avoid confusion. Sect. 3 contains some remarks on the numerical codes that have been used to generate the results in this report.

In Sect. 4 the results of the ideal MHD stability analysis of equilibria with monotonic q-profiles are presented. Here, an aspect ratio ϵ^{-1} of 5.6 has been considered and the shape of the poloidal cross-section is given by an ellipticity of 1.8 and a triangularity of 0.6. A total plasma current (dimensionless) of 0.838 is considered which corresponds to a magnetic field of 3 T and a plasma current $I_p = 500\,\mathrm{kA}$. These are typical parameter values for the KT-2 tokamak [1] which leave a lot of freedom for the equilibrium profiles. In fact, the only restriction is to keep $q_0 > 1$ in order to avoid internal kink instabilities. Starting from four ballooning stable 'reference equilibria' with ever broader pressure profiles, the effect of the shape of the poloidal plasma cross-section (ellipticity and triangularity), the aspect ratio, and the total plasma current on the ballooning stability is studied. For the same reference equilibria, the effect of the wall position, the variation of the total current, the plasma beta, the shape of the cross-section, and the aspect ratio on the growth rates of external kink modes is studied. Particular attention is given to effects that lead to stabilization with respect to these external modes.

Section 5 contains results on dissipative MHD instabilities. The effect of resistivity on the growth rates and stability thresholds of both external and internal kink instabilities is investigated. Also, thermal instabilities, the so-called MARFEs, have been calculated.

The study of 'advanced tokamak scenarios' for typical KT-2 parameters is presented in Sect. 6. Here, a local profile optimization study is performed for a lower total current, viz. $\bar{I} = 0.754$ which corresponds to $I_p = 300\,\mathrm{kA}$ and a magnetic field of 2 T. Starting from a given current density profile, the pressure profile is made marginally ballooning stable. Next, we tried to find so-called 'infernal modes' which are beleived to be responsible for the sudden collapse observed in similar JET experiments with a rearrangement of the plasma current resulting in a monotonic safety factor profile [15]. Instabilities are indeed found but they turn out to be external modes. This is shown by studying the effect of the position of the perfectly conducting wall surrounding the plasma on the growth rate of the instability. The effect of the triangularity of the poloidal cross-section of the plasma on this instability is also investigated.

Furthermore, the numerical codes HBT, CASTOR, and HELENA, and all non-standard auxiliary programs and libraries have been installed on the Cray computer used by KAERI staff. An installation and user guide has been written for HELENA [7] and for CASTOR [8].

Finally, the conclusions are summerized in Sect. 8.

2 Equilibria and definitions

The axisymmetric toroidal equilibria studied in this report are determined by the inverse aspect ratio ϵ, the shape of the poloidal cross-section of the outer flux surface, two unit input profiles $\Pi(\bar{\psi})$ and $\Gamma(\bar{\psi})$, the total current $\bar{I}$ and the plasma beta β. A schematic represention of the poloidal cross section is shown in Fig. 1.

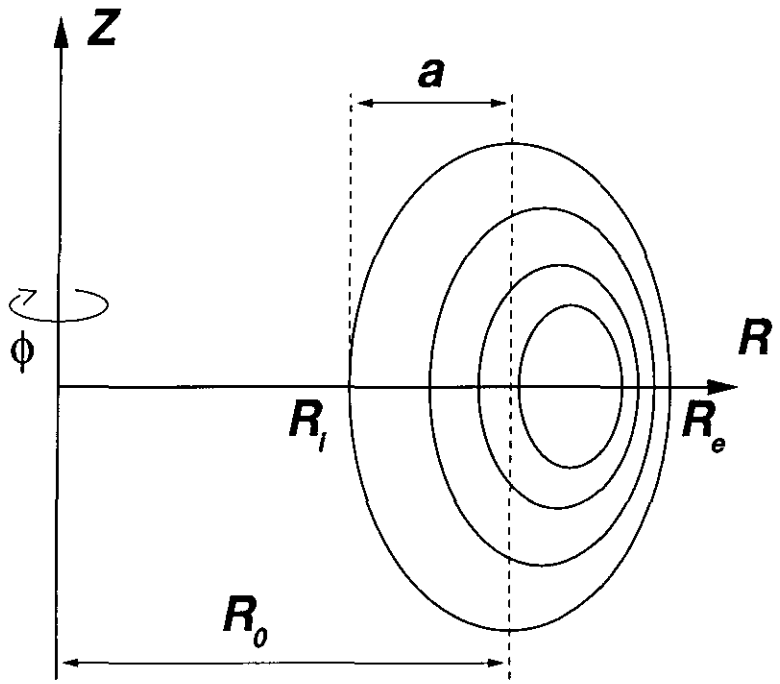

Figure 1: Schematic representation of tokamak geometry with cylindrical coordinates (R, ϕ, Z). R_e and R_i are the two values of the major radius where the last closed magnetic surface crosses the equatorial plane, where $R_i < R_e$; $a = (R_e - R_i)/2$ and $R_0 = (R_e + R_i)/2$.

The inverse aspect ratio is given by:

$$\epsilon = a/R_0, \tag{1}$$

where a and R_0 denote the minor and major radius of the plasma, respectively (see also Fig. 1). The shape of the poloidal cross-section of the outer flux surface is characterized by its ellipticity, $E = b/a$, and its triangularity, τ, according to the formula:

$$\begin{aligned} x &= a\cos(\gamma + \tau\sin(\gamma)), \\ y &= b\sin(\gamma), \end{aligned} \tag{2}$$

where x and y are the normalized coordinates, $x = (R - R_0)/a$ and $y = Z/a$, while γ denotes a poloidal angle.

The formulation of the equilibrium problem of finding $\psi(R, Z)$ in terms of physical quantities contains two trivial scaling parameters, viz. the vacuum magnetic field B_0 at the geometric center of the plasma and the scale length of the problem: a, the minor radius of the plasma boundary. These two parameters only provide the dimensions of the

physical quantities and do not enter the problem otherwise. Similarly, the total poloidal flux, $2\pi\psi_1$, only enters as a scaling parameter normalizing the J_ϕ and B_ϕ profiles. This scaling is accounted for by the parameter $\alpha = a^2 B_0/\psi_1$. The pressure profile $P(\psi)$ and the diamagnetic profile $F(\psi) = RB_\phi$ are then normalized as follows:

$$\bar{P}(\bar{\psi}) = \left(\frac{\mu_0 \alpha^2}{\epsilon B_0^2}\right) P(\psi), \qquad \bar{F}^2(\bar{\psi}) = \left(\frac{\epsilon \alpha^2}{a^2 B_0^2}\right) (F^2(\psi) - R_0^2 B_0^2), \tag{3}$$

where the nomalized flux, $\bar{\psi} = \psi/\psi_1$, will now play the role of a radial coordinate.

In both HELENA and HBT the *shape* of the two input profiles $\bar{P}(\bar{\psi})$ and $\bar{F}\bar{F}'(\bar{\psi})$ is separated from the *amplitude* by the definition of the two unit input profiles

$$\begin{aligned} \frac{1}{2} AB\Pi(\bar{\psi}) &= -\bar{P}'(\bar{\psi}), \\ A\Gamma(\bar{\psi}) &= -\frac{1}{\epsilon}(\bar{P}'(\bar{\psi}) + \bar{F}\bar{F}'(\bar{\psi})), \end{aligned} \tag{4}$$

with $\Pi(0) = \Gamma(0) = 1$. The definitions 5 of the $\Pi(\bar{\psi})$ and $\Gamma(\bar{\psi})$ profiles is the same in both the HBT equilibrium and ballooning stability code [4, 10] and the equilbrium code HELENA [7]. In terms of $\Pi(\bar{\psi})$ and $\Gamma(\bar{\psi})$ the Grad-Shafranov equation is written as follows:

$$\Delta^* \bar{\psi} = \frac{\partial^2 \bar{\psi}}{\partial x^2} + \frac{\partial^2 \bar{\psi}}{\partial y^2} - \frac{\epsilon}{1+\epsilon x} \frac{\partial \bar{\psi}}{\partial x} = A[\Gamma(\bar{\psi}) + Bx(1 + \frac{\epsilon x}{2})\,\Pi(\bar{\psi})]. \tag{5}$$

The quantities A and B determine the amplitudes of the two input profiles where only B is an input quantity (for HELENA [7]) as the value of A is determined by the condition that $\bar{\psi} = 1$ on the plasma boundary. In HBT, on the contrary, the quantity B is an output parameter and the position of the magnetic axis is specified as an input parameter δ, while A is again determined by the condition that $\bar{\psi} = 1$ on the plasma boundary.

Different definitions of the plasma beta and the normalized plasma current are used in the literature when reporting both numerical and experimental results. To avoid confusion, the definitions applied in this report are given below. In this report, the following (dimensionless) parameters are used to further characterize the equilibria:

$$\bar{I} \equiv \frac{\mu_0}{a[m]B_0[T]}\, I_p[A] \tag{6}$$

$$\beta \equiv \frac{2\epsilon}{\alpha^2} < \bar{P} > \tag{7}$$

$$\beta_p \equiv \frac{8\pi \bar{S} < \bar{P} >}{\bar{I}^2} \tag{8}$$

$$g \equiv \frac{a[m]B_0[T]}{I_p[MA]}\, \beta(\%) \tag{9}$$

$$g_N \equiv 100\, \frac{\beta}{\bar{I}} \tag{10}$$

where $\bar{S}$ is the (dimensionless) area of the poloidal cross section of the plasma and $\alpha = a^2 B_0/\psi_1$ [7]. The definitions of g and g_N are taken from reference [2].

3 Numerical methods and codes

For the study of the MHD stability of the KT-2 tokamak plasma three numerical codes have been used. Stability thresholds and linear growth rates of low-n ideal and resistive MHD instabilities are calculated numerically by means of the linear, resistive MHD code CASTOR (Complex Alfvén Spectrum for TORoidal plasmas) version 9e [6, 3, 8], which is presently exploited at the FOM-Instituut voor Plasmafysica (The Netherlands) and JET Joint Undertaking (United Kingdom) for a wide range of problems (such as internal and external, ideal and resistive instabilities, the plasma response due to an external driving antenna, and the damping of toroidicity-induced Alfvén eigenmodes or gap modes [9]. An extension of CASTOR which includes thermal effects [12] has been used to calculate the MARFEs.

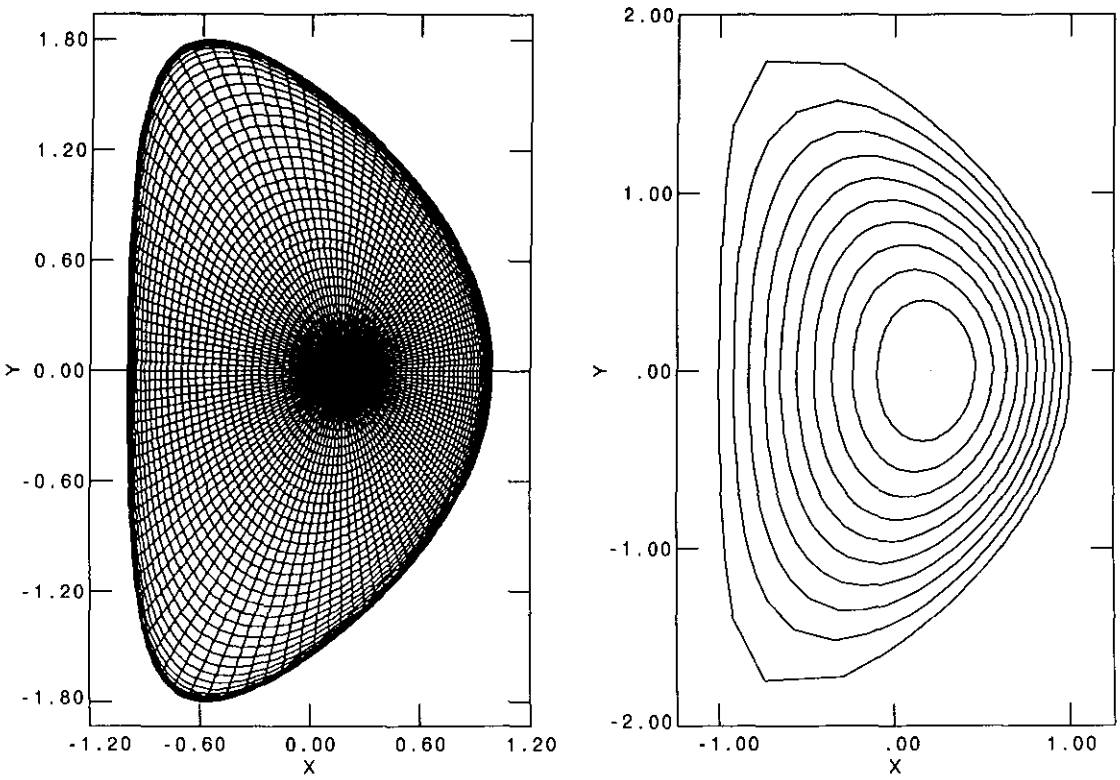

Figure 2: Typical grid produced by HELENA (left) with 41 radial grid points and 65 poloidal grid points; and typical flux surfaces produced by HBT (right) with 50 radial grid points (only 10 flux surfaces are plotted) and 128 poloidal grid points.

The ballooning stability analysis has been performed by means of the ideal-MHD stability code HBT (version 3e) (High-Beta Tokamak) [10]. In this version it is possible to use a flux surface averaged toroidal current density profile as input for the equilibrium construction. This possibility has been exploited in the pressure profile optimization for equilibria with inverted q-profiles presented in this report.

The toroidal, axisymmetric equilibria and the corresponding equilibrium mappings, required as input for CASTOR, are generated by means of the finite element code HELENA (version 8b) [5, 7] on the basis of the available design parameters of the large-aspect-ratio divertor tokamak KT-2 [1]. Hence, the MHD equilibrium code HELENA has been used as an interface between the two stability codes HBT and CASTOR by using the output from HBT to calculate the geometric quantities needed as input for CASTOR. Remark that in this process the equilibrium is reconstructed by HELENA which implies that for the kink mode stability analysis a better resolution is exploited. Typical grids and flux surfaces produced by both HBT and HELENA are shown in Fig. 2.

4 Monotonic q-profiles - ideal MHD instabilities

In this section, the 'reference equilibria' considered are characterized by the following values of the parameters: aspect ratio $\epsilon^{-1} = 5.6$, ellipticity 1.8, triangularity 0.6, plasma current $I_p = 500\,\mathrm{kA}$, and magnetic field $B_0 = 3\,\mathrm{T}$, yielding a dimensionless total current of $\bar{I} = 0.838$. Starting from ballooning stable equilibria the ideal external kink stability limits are determined for a wide range of input profiles and the effect of several parameters, e.g. the aspect ratio, the total current, and the plasma shape, on the ideal MHD stability is investigated.

4.1 Ballooning instabilities

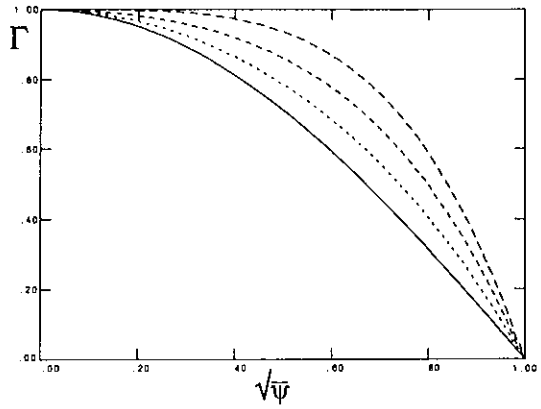

Figure 3: The range of $\Gamma(\bar{\psi})$ input profiles considered in the global optimization study for given $\Pi(\bar{\psi})$-profiles.

4.1.1 Ballooning stable equilibria

In the present study, all HBT equilibria are obtained with a resolution of 50×128. For the ballooning stability calculations, the resolution is increased to 95×256 and the plasma is 'truncated' to the range $0 \leq \bar{\psi} \leq 0.95$. The above-mentioned parameters characterizing the KT-2 tokamak plasmas leave a lot of freedom for the two input profiles $\Pi(\bar{\psi})$ and $\Gamma(\bar{\psi})$. As a matter of fact, the only restriction is that $\bar{I} = 0.838$ with q_0 slightly higher than unity. In order to get an idea of the plasma beta's one gets for the rather extreme aspect ratio, ellipticity, and triangularity characterizing the KT-2 equilibria, four different pressure profiles are considered. These are obtained by the input $\Pi(\bar{\psi})$-profiles $1 - \bar{\psi}$, $1 - \bar{\psi}^2$, $1 - \bar{\psi}^3$, and $1 - \bar{\psi}^4$, respectively, yielding an ever broader $\bar{P}(\bar{\psi})$-profile.

For each of these four Π-profiles we played around with the Γ-profile to get a total current of $\bar{I} = 0.838$ and a q_0-value above unity. We considered $\Gamma(\bar{\psi})$ profiles of the form $1 + a_\gamma\bar{\psi} + b_\gamma\bar{\psi}^2 + c_\gamma\bar{\psi}^3 + d_\gamma\bar{\psi}^4$ and varied the coefficients a_γ, b_γ, c_γ, and d_γ. In this parameter scan, the most satisfactory results (highest plasma beta's) were obtained with $\Gamma(\bar{\psi})$-profiles of the form

$$\Gamma(\bar{\psi}) = 1 + b_\gamma\bar{\psi}^2 + d_\gamma\bar{\psi}^4, \tag{11}$$

where $d_\gamma = -1 - b_\gamma$ in order to get $\Gamma(1) = 0$. The parameter b_γ was varied between -1.2 and 0.2 yielding the $\Gamma(\bar{\psi})$-profiles displayed in Fig. 3.

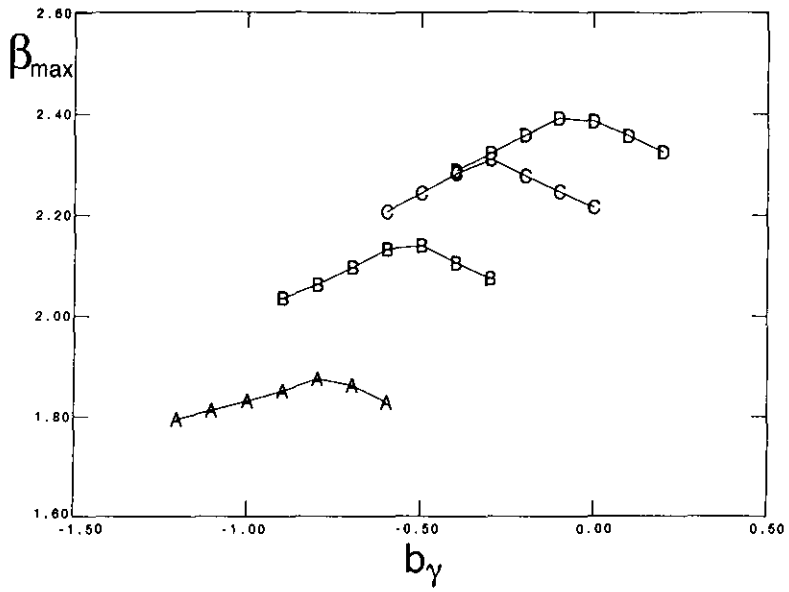

Figure 4: The maximal plasma beta (in %) that yields ballooning stability versus the input parameter b_γ for the four different pressure profiles. The labels on the curves refer to the reference equilibria A, B, C, and D, i.e. reference equilibrium A corresponds to the maximum on curve A, equilibrium B to the maximum on curve B, etc.

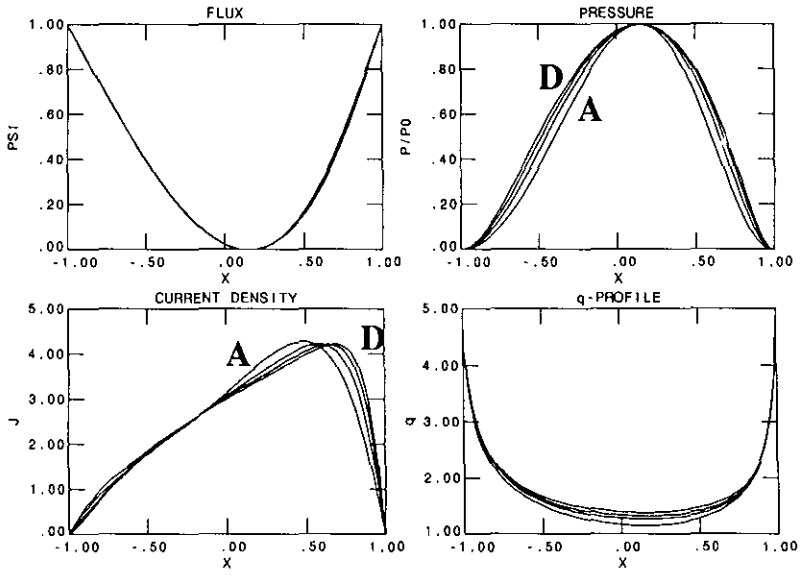

Figure 5: The $\bar{\psi}$, $\bar{P}(\bar{\psi})$, $J_\phi(\bar{\psi})$, and $q(\bar{\psi})$-profiles for the equilibria that yield maximum β for four different pressure profiles.

Code	Π-profile	Γ-profile	δ	q_0	q_1	β (%)	g	g_N
A	$1-\bar{\psi}$	$1-0.8\bar{\psi}^2-0.2\bar{\psi}^4$	.1520	1.162	4.799	1.875	2.812	2.238
B	$1-\bar{\psi}^2$	$1-0.5\bar{\psi}^2-0.5\bar{\psi}^4$	.1557	1.273	4.815	2.141	3.211	2.555
C	$1-\bar{\psi}^3$	$1-0.3\bar{\psi}^2-0.7\bar{\psi}^4$	.1540	1.331	4.859	2.312	3.466	2.758
D	$1-\bar{\psi}^4$	$1-0.1\bar{\psi}^2-0.9\bar{\psi}^4$	.1515	1.391	4.867	2.393	3.588	2.856

Table 1: The equilibria that yield maximum β for four different pressure profiles. All four equilibria have $\epsilon = 0.17857$ ($\epsilon^{-1} = 5.6$) and $\bar{I} = 0.838$ ($B = 3\,\mathrm{T}$ and $I_p = 500\,\mathrm{kA}$). The shape of the poloidal cross-section is characterized by $b/a = 1.8$ and $\tau = 0.6$.

For each of these input profiles the magnetic axis was shifted outwards (by increasing the input parameter δ) in order to find the maximum beta for each profile. The result is displayed in Fig. 4 where the plasma beta is plotted versus the parameter b_γ for the four reference Π-profiles.

The four ballooning stable equilibria with the highest β-values are summarized in Table 1 and the profiles of these four equilibria are displayed in Fig. 5. For each of these equilibria a larger horizontal shift of the magnetic axis, i.e. a larger value of δ, results in at least one ballooning unstable magnetic surface.

Remark that an ellipticity of $b/a = 1.8$, typical for the KT-2 equilibrium, is close to the limit HBT can handle. Even with a poloidal resolution of 64 grid points, the conformal mapping technique applied in HBT yields a highly nonuniform distribution of the mesh points so that the upper and lower parts of the outer flux surfaces remain poorly resolved in this direction. Doubling the resolution to 128 does not solve this problem since most of the additional grid points are mapped close to the horizontal ($z = 0$) plane as shown in Fig. 2.

4.1.2 Effect of the ellipticity of the cross-section

The effect of the ellipticity of the poloidal cross-section on the marginal ballooning stable plasma beta has been investigated for each of the four reference equilibria mentioned above. The ellipticity was varied from 1.4 to 1.9 while keeping the input profiles and all other parameters fixed, except for the horizontal shift of the magnetic axis, δ. For each of the equilibria, the magnetic axis was shifted outwards up to the point where a ballooning instability occured on at least one magnetic flux surface. The results are summarized in Table 2 with the shift of the magnetic axis in the second column and the corresponding β_p, β, g_N, q_0, and q_1 in columns 3, 4, 5, 6, and 7, respectively. These equilibria are 'marginally' ballooning stable in the sense that a further increase of the pressure, i.e. a larger value of δ, yields at least one ballooning unstable magnetic surface. The last column of Table 2 contains the position of the innermost magnetic surface that becomes ballooning unstable when the magnetic axis is shifted further outward than δ_{max}.

From Table 2 it is clear that as b/a decreases, q_0 and q_1 both decrease. But q_1 decreases

Equilibrium A							
b/a	δ_{max}	$\beta_{p\,max}$	β_{max}	g_N	q_0	q_1	ψ_{inst}
1.9	0.1629	1.893	1.853	2.211	1.207	5.320	0.34
1.8	0.1520	1.814	1.874	2.236	1.162	4.862	0.34
1.7	0.1390	1.716	1.878	2.242	1.120	4.246	0.34
1.6	0.1239	1.604	1.865	2.226	1.080	3.702	0.34
1.5	0.1060	1.472	1.827	2.180	1.042	3.275	0.35
1.4	0.0851	1.325	1.761	2.101	1.004	2.868	0.35
Equilibrium B							
b/a	δ_{max}	$\beta_{p\,max}$	β_{max}	g_N	q_0	q_1	ψ_{inst}
1.9	0.1684	2.220	2.172	2.592	1.314	5.482	0.47
1.8	0.1557	2.102	2.172	2.592	1.265	4.893	0.47
1.7	0.1411	1.968	2.153	2.570	1.219	4.265	0.48
1.6	0.1243	1.816	2.112	2.520	1.175	3.709	0.48
1.5	0.1047	1.645	2.041	2.436	1.132	3.275	0.46
1.4	0.0821	1.458	1.939	2.314	1.090	2.863	0.47
Equilibrium C							
b/a	δ_{max}	$\beta_{p\,max}$	β_{max}	g_N	q_0	q_1	ψ_{inst}
1.9	0.1668	2.383	2.332	2.783	1.380	5.458	0.61
1.8	0.1540	2.252	2.327	2.777	1.327	4.935	0.60
1.7	0.1390	2.100	2.298	2.743	1.278	4.290	0.58
1.6	0.1215	1.925	2.239	2.672	1.232	3.725	0.58
1.5	0.1014	1.734	2.154	2.571	1.187	3.278	0.57
1.4	0.0784	1.528	2.031	2.423	1.144	2.865	0.56
Equilibrium D							
b/a	δ_{max}	$\beta_{p\,max}$	β_{max}	g_N	q_0	q_1	ψ_{inst}
1.9	0.1644	2.463	2.412	2.878	1.443	5.404	0.69
1.8	0.1515	2.324	2.400	2.865	1.388	4.927	0.69
1.7	0.1364	2.162	2.367	2.824	1.337	4.291	0.68
1.6	0.1188	1.978	2.300	2.745	1.289	3.728	0.66
1.5	0.0985	1.775	2.202	2.628	1.242	3.264	0.66
1.4	0.0753	1.557	2.070	2.470	1.196	2.859	0.65

Table 2: Effect of the ellipticity on the marginal ballooning stability limit for the four reference equilibria. The triangularity of the cross-section, the aspect ratio, the total current, and the profiles are fixed. The displayed parameter values correspond to marginal ballooning stable equilibria.

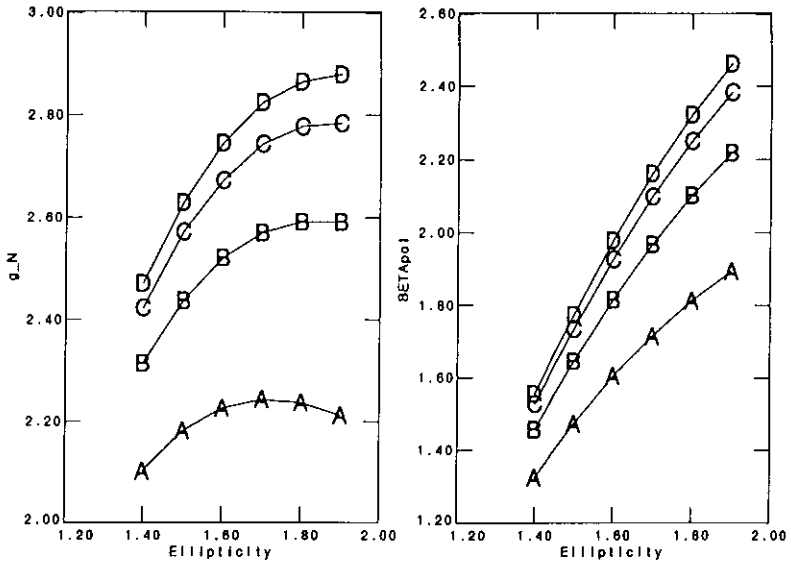

Figure 6: The normalized plasma beta, g_N, and poloidal beta, β_p, versus the ellipticity of the plasma cross-section for the four reference equilibria with $\epsilon = 0.17857$ ($\epsilon^{-1} = 5.6$) and $\bar{I} = 0.838$ ($B = 3\,\mathrm{T}$ and $I_p = 500\,\mathrm{kA}$). The triangularity of the cross-section is 0.6. The plotted values yield marginal ballooning stability.

faster than q_0 so that $q_1 - q_0$, the average shear, decreases with decreasing ellipticity. The maximal shift of the magnetic axis, δ_{max}, also decreases monotonically with decreasing ellipticity for all four equilibria. However, the corresponding marginal plasma beta, β_{max}, decreases monotonically for Equilibria C and D, but for Equilibrium A and B it first increases and than decreases again as the ellipticity is decreased from 1.9 to 1.4. In the ellipticity scan, β_{max} varies from 6.4% for equilibrium A to 16% for equilibrium D. In Fig. 6 the normalized beta, g_N, is plotted versus the ellipticity. From this plot it is clear that g_N is close to optimal for $b/a = 1.8$, and this holds for all four reference equilibria.

The marginal poloidal plasma beta, β_{pmax}, increases monotonically with increasing ellipticity, see also Fig. 6. The relative change of β_{pmax} in the ellipticity scan is larger than the relative change of β_{max}: β_{pmax} changes by 43% for equilibrium A and by 58% for equilibrium D. The position of the innermost ballooning instability does not depend significantly on the ellipticity of the plasma cross-section.

4.1.3 Effect of the triangularity of the cross-section

The effect of the triangularity of the poloidal cross-section on the marginal ballooning stable plasma beta has also been investigated for each of the four reference equilibria mentioned above. The triangularity τ was varied from 0.2 to 0.7. For each of the equilibria, the magnetic axis was again shifted outwards up to the point where a ballooning instability occured on at least one magnetic flux surface. The results are summarized in Table 3 with the marginally stable shift of the magnetic axis in the second column and the corresponding marginal β_p, β, g_N, q_0, and q_1 in columns 3, 4, 5, 6, and 7, respectively.

The last column of Table 3 contains the position of the innermost magnetic surface that becomes ballooning unstable when the magnetic axis is shifted further outward than δ_{max}.

From Table 3 it is clear that as τ decreases, q_0 increases and q_1 decrease. Hence, $q_1 - q_0$ decreases with decreasing triangularity. The marginal plasma beta, β_{max}, first increases with increasing triangularity and then decreases again. This is so for all four reference equilibria. The relative change of β_{max} is somewhat larger than for the ellipticity scan discussed above: from 19% for equilibrium A to 25% for equilibrium D. Moreover, the optimal value is obtained for $\tau = 0.6$ for all four equilibria, as can be seen in Fig. 7.

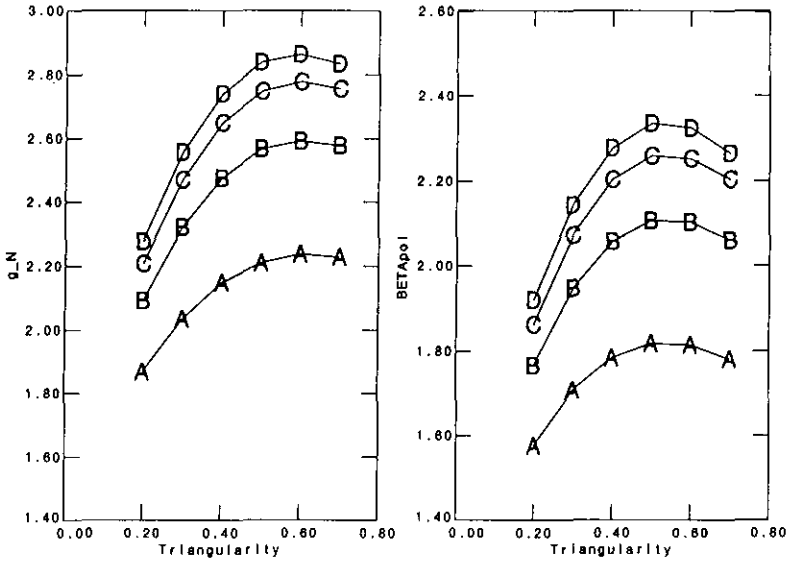

Figure 7: The normalized plasma beta, g_N, and beta poloidal, β_p, versus the triangularity of the plasma cross-section for the four reference equilibria with $\epsilon = 0.17857$ ($\epsilon^{-1} = 5.6$) and $\bar{I} = 0.838$ ($B = 3\,\mathrm{T}$ and $I_p = 500\,\mathrm{kA}$). The ellipticity of the cross-section is 1.8. The plotted values yield marginal ballooning stability.

The marginal ballooning stable poloidal plasma beta, $\beta_{p\,max}$, also first increases with increasing triangularity and then decreases again, see also Fig. 7. The relative change of $\beta_{p\,max}$ in this triangularity scan is much smaller than that in the ellipticity scan discussed in the previous subsection. Here $\beta_{p\,max}$ varies from 13% for equilibrium A to 18% for equilibrium D. The position of the innermost ballooning instability does not depend significantly on the triangularity of the plasma cross-section.

4.1.4 Effect of the aspect ratio

The effect of the aspect ratio on the marginal ballooning stable plasma beta has also been investigated for each of the four reference equilibria discussed in Sect. 4.1.1. The aspect ratio R_0/a has been varied from 4.0 to 6.0. Again, for each of the equilibria the magnetic axis was shifted outwards up to the point where a ballooning instability occured on at least one magnetic flux surface. The results are summarized in Table 4 with the marginally stable shift of the magnetic axis in the second column and the corresponding

Equilibrium A							
τ	δ_{max}	$\beta_{p\,max}$	β_{max}	g_N	q_0	q_1	ψ_{inst}
0.7	0.1434	1.780	1.866	2.227	1.127	5.502	0.34
0.6	0.1520	1.814	1.874	2.236	1.162	4.862	0.34
0.5	0.1584	1.818	1.853	2.211	1.205	4.376	0.33
0.4	0.1622	1.784	1.799	2.147	1.260	4.016	0.33
0.3	0.1629	1.707	1.706	2.035	1.325	3.748	0.34
0.2	0.1598	1.576	1.566	1.868	1.403	3.533	0.35
Equilibrium B							
τ	δ_{max}	$\beta_{p\,max}$	β_{max}	g_N	q_0	q_1	ψ_{inst}
0.7	0.1467	2.059	2.159	2.576	1.224	5.465	0.46
0.6	0.1557	2.102	2.172	2.592	1.265	4.893	0.47
0.5	0.1622	2.106	2.151	2.567	1.317	4.379	0.47
0.4	0.1654	2.058	2.074	2.475	1.384	4.030	0.49
0.3	0.1647	1.947	1.945	2.321	1.466	3.747	0.48
0.2	0.1593	1.765	1.753	2.092	1.562	3.518	0.47
Equilibrium C							
τ	δ_{max}	$\beta_{p\,max}$	β_{max}	g_N	q_0	q_1	ψ_{inst}
0.7	0.1446	2.203	2.309	2.755	1.282	5.585	0.60
0.6	0.1540	2.252	2.327	2.777	1.327	4.935	0.60
0.5	0.1608	2.259	2.303	2.748	1.384	4.415	0.58
0.4	0.1640	2.202	2.220	2.649	1.457	4.042	0.58
0.3	0.1629	2.072	2.071	2.471	1.546	3.749	0.58
0.2	0.1568	1.863	1.850	2.208	1.652	3.511	0.57
Equilibrium D							
τ	δ_{max}	$\beta_{p\,max}$	β_{max}	g_N	q_0	q_1	ψ_{inst}
0.7	0.1415	2.265	2.377	2.836	1.342	5.544	0.68
0.6	0.1515	2.324	2.400	2.865	1.388	4.927	0.69
0.5	0.1587	2.335	2.380	2.840	1.447	4.425	0.68
0.4	0.1622	2.277	2.295	2.740	1.524	4.037	0.68
0.3	0.1615	2.144	2.143	2.557	1.619	3.743	0.66
0.2	0.1552	1.920	1.907	2.276	1.733	3.501	0.65

Table 3: Effect of the triangularity on the marginal ballooning stability limit for the four reference equilibria. The aspect ratio, the total current, the ellipticity, and the profiles are fixed. The displayed parameter values correspond to marginal ballooning stable equilibria.

marginal β_p, β, g_N, q_0, and q_1 in columns 3, 4, 5, 6, and 7, respectively. The last column of Table 4 contains the position of the innermost magnetic surface that becomes ballooning unstable when the magnetic axis is shifted further outward than δ_{max}.

From Table 4 it is clear that as R_0/a decreases, q_0 and q_1 both increase. However, q_1 increases faster than q_0 so that $q_1 - q_0$ increases with decreasing aspect ratio. The marginal plasma beta, β_{max}, increases almost linearly with the aspect ratio, as can be seen in Fig. 8. This is so for all four reference equilibria. An increase of the aspect ratio reduces the bending of the magnetic surfaces so that the plasma becomes less susceptible to ballooning instabilities. The relative change of β_{max} in this aspect ratio scan is roughly the same for the four reference equilibria, viz. about 8%.

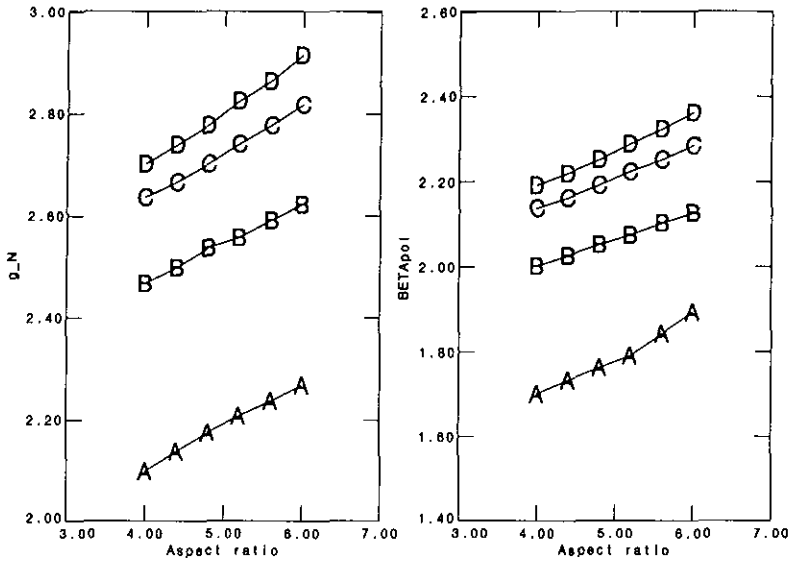

Figure 8: The normalized plasma beta, g_N, and beta poloidal, β_p, versus the aspect ratio of the plasma for the four reference equilibria with $\epsilon = 0.17857$ ($\epsilon^{-1} = 5.6$) and $\bar{I} = 0.838$ ($B = 3\,\mathrm{T}$ and $I_p = 500\,\mathrm{kA}$). The triangularity of the cross-section is 0.6 and the ellipticity 1.8. The plotted values yield marginal ballooning stability.

The marginal poloidal plasma beta, $\beta_{p\,max}$, also increases almost linearly with increasing aspect ratio, see also Fig. 8. As for β_{max}, the relative change of $\beta_{p\,max}$ in this aspect ratio scan is roughly the same for the four reference equilibria, viz. about 8%. The position of the innermost ballooning instability depends slightly on the aspect ratio, in particular for Equilibria C and D. The first ballooning unstable flux surface shifts inwards as the aspect ratio is increased.

4.1.5 Effect of the total plasma current

The effect of the total current on the marginal ballooning stable plasma beta has been investigated for each of the four reference equilibria mentioned above. The total plasma current $\bar{I}$ was varied from 0.5027 to 0.9215. For a fixed magnetic field strength of 3 Tesla this corresponds to a range from 300 kA to 550 kA as indicated in the first column of

Equilibrium A							
R_0/a	δ_{max}	$\beta_{p\,max}$	β_{max}	g_N	q_0	q_1	ψ_{inst}
6.0	0.1419	1.839	1.900	2.268	1.111	4.329	0.33
5.6	0.1520	1.814	1.874	2.236	1.162	4.862	0.34
5.2	0.1635	1.790	1.850	2.207	1.215	5.352	0.33
4.8	0.1762	1.762	1.822	2.174	1.272	5.832	0.34
4.4	0.1905	1.732	1.790	2.137	1.331	6.767	0.34
4.0	0.2069	1.701	1.758	2.098	1.393	7.614	0.35
Equilibrium B							
R_0/a	δ_{max}	$\beta_{p\,max}$	β_{max}	g_N	q_0	q_1	ψ_{inst}
6.0	0.1453	2.127	2.198	2.623	1.209	4.356	0.46
5.6	0.1557	2.102	2.172	2.592	1.265	4.893	0.47
5.2	0.1672	2.075	2.143	2.557	1.326	5.401	0.48
4.8	0.1807	2.052	2.121	2.537	1.390	5.985	0.49
4.4	0.1956	2.026	2.093	2.498	1.458	6.918	0.51
4.0	0.2130	2.001	2.067	2.467	1.527	7.819	0.51
Equilibrium C							
R_0/a	δ_{max}	$\beta_{p\,max}$	β_{max}	g_N	q_0	q_1	ψ_{inst}
6.0	0.1441	2.285	2.362	2.818	1.266	4.370	0.58
5.6	0.1540	2.252	2.327	2.777	1.327	4.935	0.60
5.2	0.1653	2.223	2.297	2.741	1.392	5.459	0.61
4.8	0.1780	2.191	2.264	2.702	1.463	5.974	0.62
4.4	0.1926	2.162	2.234	2.666	1.537	6.972	0.63
4.0	0.2098	2.137	2.209	2.636	1.612	7.855	0.63
Equilibrium D							
R_0/a	δ_{max}	$\beta_{p\,max}$	β_{max}	g_N	q_0	q_1	ψ_{inst}
6.0	0.1421	2.363	2.442	2.915	1.323	4.368	0.66
5.6	0.1515	2.324	2.400	2.865	1.388	4.927	0.69
5.2	0.1622	2.288	2.368	2.825	1.458	5.456	0.69
4.8	0.1744	2.251	2.327	2.777	1.543	5.972	0.70
4.4	0.1887	2.220	2.294	2.738	1.613	6.995	0.71
4.0	0.2052	2.191	2.264	2.702	1.695	7.987	0.72

Table 4: Effect of the aspect ratio on the marginal ballooning stability limit for the four reference equilibria. The shape of the cross-section, the total current, and the profiles are fixed. The displayed parameter values correspond to marginal ballooning stable equilibria.

Table 5. Table 5 further contains the marginally stable shift of the magnetic axis in the second column and the corresponding marginal β_p, β, g_N, q_0, and q_1 in columns 3, 4, 5, 6, and 7, respectively. The last column of Table 5 contains the position of the innermost magnetic surface that becomes ballooning unstable when the magnetic axis is shifted further outward than δ_{max}.

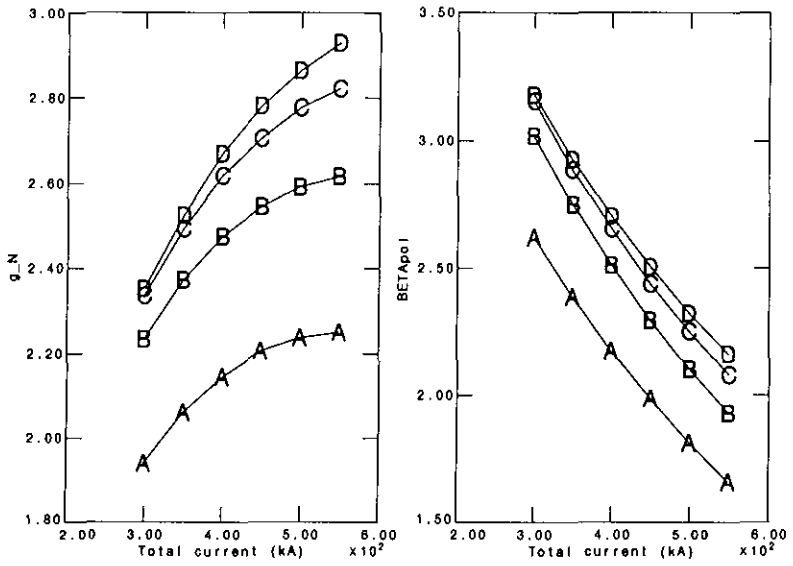

Figure 9: The normalized plasma beta, g_N, and beta poloidal, β_p, versus the total plasma current for the four reference equilibria with $\epsilon = 0.17857$ ($\epsilon^{-1} = 5.6$). The triangularity of the cross-section is 0.6 and the ellipticity 1.8. The plotted values yield marginal ballooning stability.

From Table 5 it is clear that as $\bar{I}$ decreases, q_0 and q_1 both increase substantially. However, q_1 increases even faster than q_0 so that $q_1 - q_0$ increases with decreasing $\bar{I}$. The marginal plasma beta, β_{max}, increases monotonically with the plasma current, as can be seen in Fig. 9. This is so for all four reference equilibria. The relative increase of β_{max} in this $\bar{I}$-scan comprises 16% for equilibrium A while it comprises 25% for equilibrium D.

However, the marginal poloidal plasma beta, $\beta_{p\,max}$, *decreases almost linearly* with increasing plasma current, see also Fig. 9. And this decrease of $\beta_{p\,max}$ with increasing plasma current is quite substantial: from 58% for equilibrium A to 47% for equilibrium D. The position of the innermost ballooning instability depends considerably on the plasma current, for all four reference equilibria. The first ballooning unstable flux surface shifts inwards as the plasma current is increased.

Equilibrium A							
$\bar{I}$	δ_{max}	$\beta_{p\,max}$	β_{max}	g_N	q_0	q_1	ψ_{inst}
0.9215 (550 kA)	0.1393	1.659	2.072	2.249	1.091	4.272	0.32
0.8380 (500 kA)	0.1520	1.814	1.874	2.236	1.162	4.862	0.34
0.7540 (450 kA)	0.1656	1.987	1.662	2.204	1.245	5.483	0.35
0.6702 (400 kA)	0.1797	2.174	1.437	2.144	1.348	6.201	0.36
0.5864 (350 kA)	0.1948	2.387	1.208	2.060	1.474	7.351	0.38
0.5027 (300 kA)	0.2106	2.622	0.975	1.940	1.639	8.608	0.39
Equilibrium B							
$\bar{I}$	δ_{max}	$\beta_{p\,max}$	β_{max}	g_N	q_0	q_1	ψ_{inst}
0.9215 (550 kA)	0.1432	1.928	2.409	2.615	1.184	4.251	0.46
0.8380 (500 kA)	0.1557	2.102	2.172	2.592	1.265	4.893	0.47
0.7540 (450 kA)	0.1690	2.296	1.920	2.546	1.362	5.509	0.48
0.6702 (400 kA)	0.1832	2.511	1.659	2.475	1.480	6.376	0.52
0.5864 (350 kA)	0.1981	2.750	1.391	2.372	1.628	7.524	0.55
0.5027 (300 kA)	0.2141	3.019	1.122	2.233	1.820	8.926	0.57
Equilibrium C							
$\bar{I}$	δ_{max}	$\beta_{p\,max}$	β_{max}	g_N	q_0	q_1	ψ_{inst}
0.9215 (550 kA)	0.1427	2.081	2.601	2.823	1.238	4.278	0.57
0.8380 (500 kA)	0.1540	2.252	2.327	2.777	1.327	4.935	0.60
0.7540 (450 kA)	0.1658	2.439	2.040	2.705	1.436	5.583	0.62
0.6702 (400 kA)	0.1790	2.655	1.755	2.618	1.565	6.314	0.63
0.5864 (350 kA)	0.1926	2.889	1.462	2.493	1.729	7.555	0.66
0.5027 (300 kA)	0.2073	3.155	1.173	2.334	1.942	8.903	0.67
Equilibrium D							
$\bar{I}$	δ_{max}	$\beta_{p\,max}$	β_{max}	g_N	q_0	q_1	ψ_{inst}
0.9215 (550 kA)	0.1413	2.161	2.701	2.931	1.292	4.288	0.66
0.8380 (500 kA)	0.1515	2.324	2.400	2.865	1.388	4.927	0.69
0.7540 (450 kA)	0.1625	2.507	2.098	2.782	1.504	5.578	0.70
0.6702 (400 kA)	0.1741	2.706	1.789	2.669	1.646	6.282	0.71
0.5864 (350 kA)	0.1865	2.928	1.481	2.525	1.825	7.577	0.73
0.5027 (300 kA)	0.1998	3.179	1.182	2.351	2.057	9.156	0.74

Table 5: Effect of the total current on the marginal ballooning stability limit for the four reference equilibria. The aspect ratio, the triangularity, the ellipticity, and the profiles are fixed. The corresponding current for a fixed magnetic field strength (3 T) are also given in the first column. The displayed parameter values correspond to marginal ballooning stable equilibria.

4.2 External kink instabilities

The four ballooning stable 'reference equilibria' (see Table 1) are unstable with respect to ideal external kink modes. For the purpose of calculating the growth rates, the four HBT equilibria summarized in Table 1 have been reconstructed with HELENA in order to get the equilibrium mappings required as input for CASTOR. In contrast to HBT, HELENA can easily handle the 'extreme' plasma elongation (1.8) and triangularity (0.6) and the resolution problem encountered by HBT does not occur with HELENA. The resolution is specified as 41 radial grid points (NR) and 129 poloidal grid points (NP) but for the mapping we specified NRMAP = 41 and NPMAP = 65. Moreover, the radial mesh is accumulated at the plasma boundary in order to resolve the steep gradients in the current density profile occuring in the outer plasma layers.

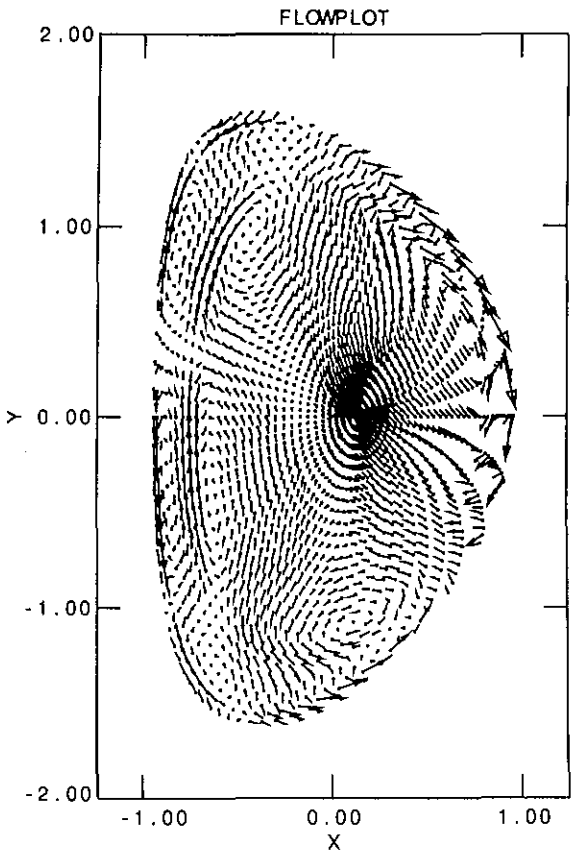

Figure 10: The velocity perturbation in a cross section of the tokamak by an ideal $n = -1$ external kink instability of reference equilibrium B.

A typical flow plot, illustrating the flow in a cross section of the tokamak, for such an external kink is shown in Fig. 10. The velocity perturbation of these external modes is localized at the edge of the tokamak plasma.

Equilibrium D has the strongest current gradient at the edge and it is the most unstable. Calculations were mainly done for the toroidal wavenumber $n = -1$, for which the most unstable solutions are expected, but the $n = -2$ instabilities were also calculated.

In the following sections, we investigate the influence of several input parameters on these instabilities. Particular attention is given to conditions that yield stable equilibria. The dimensionless growth rate is defined as

$$\mathrm{Re}(\lambda) \equiv \mathrm{Re}\left(\frac{i\omega}{\tau_A}\right), \tag{12}$$

with τ_A the Alfvén transit time

$$\tau_A \equiv \frac{R_M\sqrt{\mu_0\rho_0}}{B_0}, \tag{13}$$

where R_M denotes the radius of the magnetic axis, and B_0 and ρ_0 denote the equilibrium toroidal field and the equilibrium plasma density at the position of the magnetic axis, respectively.

4.2.1 Convergence study

The kink instability is a global mode so that good convergence in growth rate and eigenfunctions is already obtained with 50 radial gridpoints. For these external modes, the high order Fourier components are not negligible for the solution in the vacuum. Convergence studies showed that as much as 16 Fourier modes need to be taken into account in order to get 'reliable' results with growth rates close to converged values. The results discussed below are obtained with the 16 Fourier components ($m = 0, 1, \ldots, 15$). A more extensive convergence study is presented for the resistive MHD instabilities.

Equilibrium Code	R_{wall}				
	10.0	2.0	1.5	1.3	1.2
A	3.64	3.04	1.98	0.53	stable
B	5.07	4.54	2.94	1.27	stable
C	6.35	4.77	3.53	1.57	stable
D	7.38	6.55	4.02	1.74	stable

Table 6: The effect of the wall position R_{wall} (normalized to the small radius a) on the growth rate of the $n = -1$ ideal external kink. The figures $\times 10^{-2}$ represent the growth rate (normalized to the Alfvén transit time) at different wall positions for the four 'reference equilibria'.

4.2.2 Effect of the wall position

The wall has a stabilizing effect on all the instabilities found. The closer the wall to the plasma, the lower the growth rate becomes (see Table 6). The instabilities are stabilized at a position $R_{wall} \approx 1.2$. This confirms that these instabilities are external modes, needing a rational surface in the external vacuum. Below, the wall position will always be fixed at 2, unless specifically mentioned otherwise. Table 6 shows that the growth rate increases

when going from reference equilibrium A to B, C and D, which can be attributed to an ever larger driving force for the instability, viz. the current gradient at the edge.

4.2.3 Effect of the total current

We varied the total current, starting from the reference equilibria with $I_p = 500\,\mathrm{kA}$. This was done in CASTOR by varying the input parameter Q0ZYL, which determines q_0, the value of the safety factor at the magnetic axis. This input parameter rescales some equilibrium parameters, but leaves the shape of the profiles, calculated by HELENA, unaffected :

$$\begin{array}{ll} I_p \propto 1/q_0 & q_1 \propto q_0 \\ \beta \propto 1/q_0^2 & \beta_p \text{ unaffected} \\ g \propto 1/q_0 & g_N \propto 1/q_0 \end{array} \tag{14}$$

The calculations show that $q_1 \propto 1/I_p$ plays a key-role for the growth rate of the kink instability. The reference equilibria have $q_1 \approx 4.8$. By lowering I_p somewhat, we can get $q_1 > 5$. This proves to be sufficient to stabilize equilibria A and B. The kinks of equilibria C and D, i.e. the most unstable equilibria with the highest current gradient at the edge, are not stabilized, but their growth rate becomes lower. Figure 11 summarizes the result of the calculations.

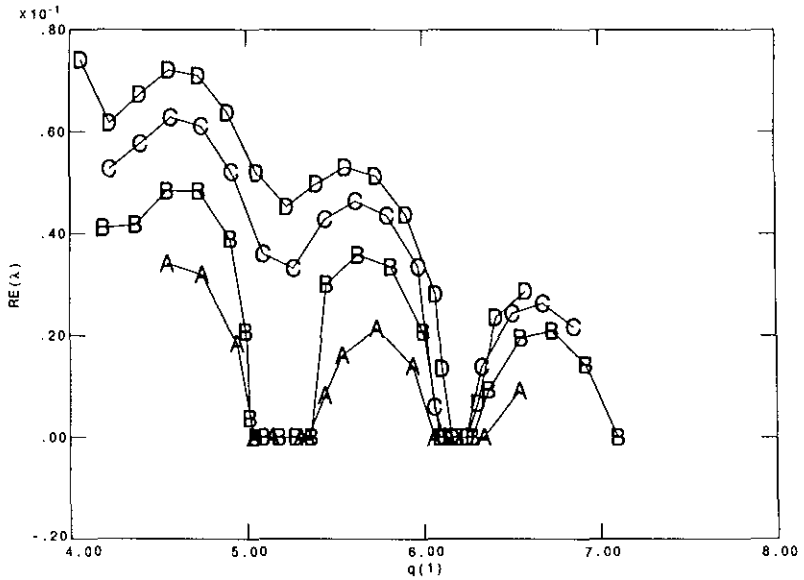

Figure 11: The normalized growth rate of the $n = -1$ ideal external kink as a function of q_1, i.e. q at the plasma boundary, for the four 'reference equilibria' (the labels on the curves refer to the equilibrium), where q_1 was varied by changing the total current I_p.

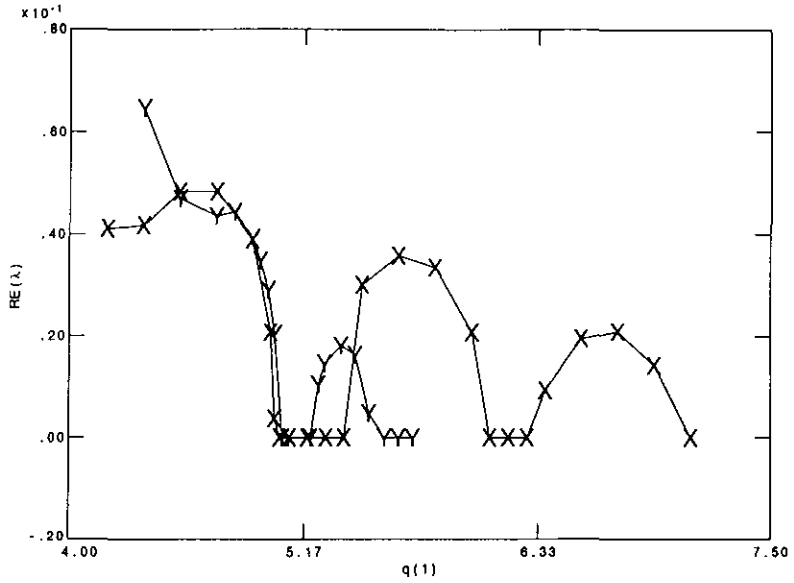

Figure 12: The normalized growth rate of the $n = -1$ (with label X) and $n = -2$ (with label Y) ideal external kink as a function of q_1, i.e. q at the plasma boundary, for equilibrium B, where q_1 was varied by changing the total current I_p.

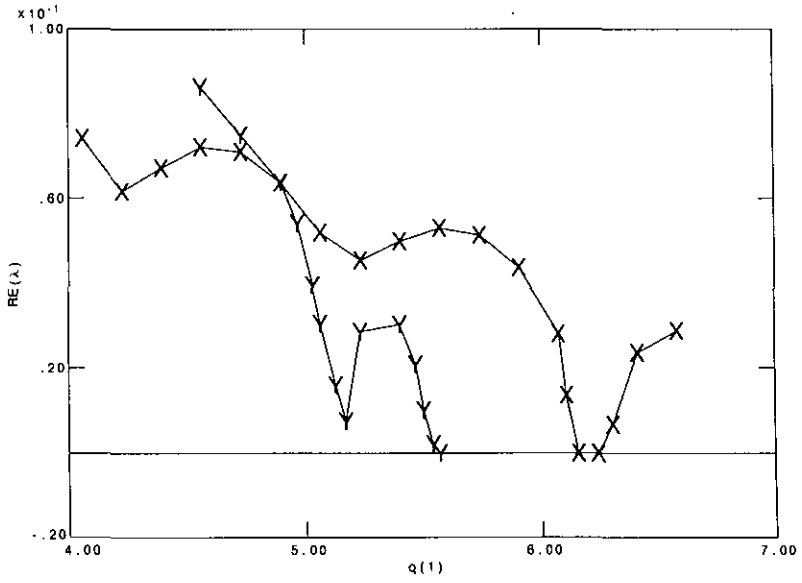

Figure 13: The normalized growth rate of the $n = -1$ (with label X) and $n = -2$ (with label Y) ideal external kink as a function of q_1, i.e. q at the plasma boundary, for equilibrium D, where q_1 was varied by changing the total current I_p.

The equilibrium with the highest β, which is still stable for external kinks, is attained from equilibrium B with $I_p = 477\,\mathrm{kA}$, where $q_1 = 5.05$, $\beta = 1.9\%$, $g = 3.03$, $g_N = 2.41$, and $q_0 = 1.34$. Current control offers a tool to maintain stable equilibria. For stability with respect to external kink modes this requires that the safety factor profile, and in particular q_1, is fixed before the plasma is heated.

The findings for the $n = -2$ instability are similar to those for the $n = -1$ instability. Figure 12 compares for equilibrium B the growth rate of the $n = -1$ and $n = -2$ instability. The $n = -2$ mode can also be stabilized by getting the rational surface $q = 5$ in the plasma. The 'window of stability' at $q_1 = 5$ is more narrow for the $n = -2$ kink, but an extra 'window of stability' is obtained at $q_1 = 5.5$. This can probably be attributed to the $(n = -2, m = 11)$ mode which becomes unstable as q_1 approaches 5.5, and which is stabilized when the rational surface $q = 11/2$ is located inside the plasma. Figure 13 compares the $n = -1$ and $n = -2$ instability for equilibrium D. The $n = -2$ instability can not be stabilized at $q_1 = 5$, in agreement with the $n = -1$ instability, but has a stability window at $q_1 = 5.5$.

Equilibrium A						
B	β_p	$\beta(\%)$	g_N	q_0	q_1	**growth rate**
1.18	1.81	1.88	2.24	1.16	4.78	3.04×10^{-2}
1.10	1.69	1.74	2.08	1.20	4.74	2.76×10^{-2}
1.00	1.53	1.58	1.89	1.24	4.66	1.94×10^{-2}
0.95	1.45	1.50	1.79	1.26	4.63	1.47×10^{-2}
0.90	1.37	1.41	1.69	1.29	4.59	stable
0.80	1.21	1.25	1.50	1.33	4.53	stable
Equilibrium D						
B	β_p	$\beta(\%)$	g_N	q_0	q_1	**growth rate**
0.860	2.31	2.39	2.86	1.39	4.87	6.55×10^{-2}
0.800	2.13	2.20	2.62	1.43	4.76	6.38×10^{-2}
0.700	1.83	1.89	2.26	1.51	4.60	4.72×10^{-2}
0.600	1.54	1.60	1.91	1.58	4.46	2.65×10^{-2}
0.550	1.40	1.46	1.73	1.61	4.40	1.19×10^{-2}
0.525	1.33	1.38	1.65	1.63	4.37	0.40×10^{-2}
0.500	1.26	1.31	1.56	1.65	4.34	stable

Table 7: The effect of plasma beta on the growth rate of the $n = -1$ ideal external kink. The growth rate is normalized to the Alfvén transit time.

4.2.4 Effect of the plasma beta

The total pressure and β can be lowered with the HELENA input parameter B, keeping the total current I_p constant. The shape of the pressure profile remains the same and the current profile becomes less peaked with a smaller gradient at the edge. Table 7 gives some figures of the calculations, showing a decrease in average shear $q_1 - q_0$ with decreasing β. Stabilization of the four reference equilibria is possible at values for β between 1.3% and 1.4% with g_N between 1.55 and 1.70, which are rather low values in comparison with those obtained with current and shape control.

4.2.5 Effect of the plasma shape and the aspect ratio

The influence of the different plasma shape parameters, i.e. triangularity, ellipticity and the aspect ratio, was investigated by changing one of these parameters, while keeping all the other input parameters of the equilibrium constant.

Table 8 gives a first impression of the influence from these shape parameters on various equilibrium parameters and the growth rate of the $n = -1$ external kink. The largest influence is seen on the value of q_1, which is a crucial value for the growth rate of the external kink.

Triangularity

Lowering the triangularity results in a lower β and g_N, while the q-profile becomes flatter, i.e. less shear (q_0 larger and q_1 smaller), but stabilization was not obtained in the scan presented in Table 8. However, this turned out to be a resolution problem. The low resolution of the triangularity scan in Table 8, with steps of 0.1 in τ, overlooks stability windows. As a matter of fact, by slightly increasing the triangularity of the reference equilibria, we can get $q_1 > 5$ and stabilize the external kinks while β is higher than the β value of the reference equilibria. Table 9 illustrates the latter for equilibrium B with a high-resolution scan of the triangularity from $\tau = 0.6$ to $\tau = 0.7$. A kink stable equilibrium is attained for $\tau = 0.65$ at $q_1 = 5.10$ with $\beta = 2.17\%$ and $g_N = 2.58$.

The same triangularity scans were done for the other reference equilibria and are presented in Figure 14. Equilibrium C can be stabilized by increasing the triangularity to $\tau = 0.65$ (and $q_1 = 5.16$), yielding $\beta = 2.34\%$ and $g_N = 2.79$, the 'best' result of our calculations on kink stability of monotonic profiles.

The variation of the triangularity offers thus a possibility to stabilize the external kink, because of its impact on q_1. Other calculations were done to study the effect of total current for different values of τ. Figure 15 compares the reference value of $\tau = 0.6$ with $\tau = 0.5$ and $\tau = 0.7$ for equilibrium B. The 'window of stability' at $q_1 > 5$ is the most wide for the reference value $\tau = 0.6$. It is remarkable that $\tau = 0.6$ proves again to be an optimal value, just like in the study of ballooning stability.

Ellipticity

The low-resolution ellipticity scan, with steps of 0.1 in b/a, presented in Table 8 is again misleading as it indicates that lower ellipticities yield higher β's, lower q_0's and q_1's but no stabilization. Again, high-resolution scans show that the external kinks can be stabilized by slightly increasing the ellipticity to get $q_1 > 5$, but this lowers β, compared to the value

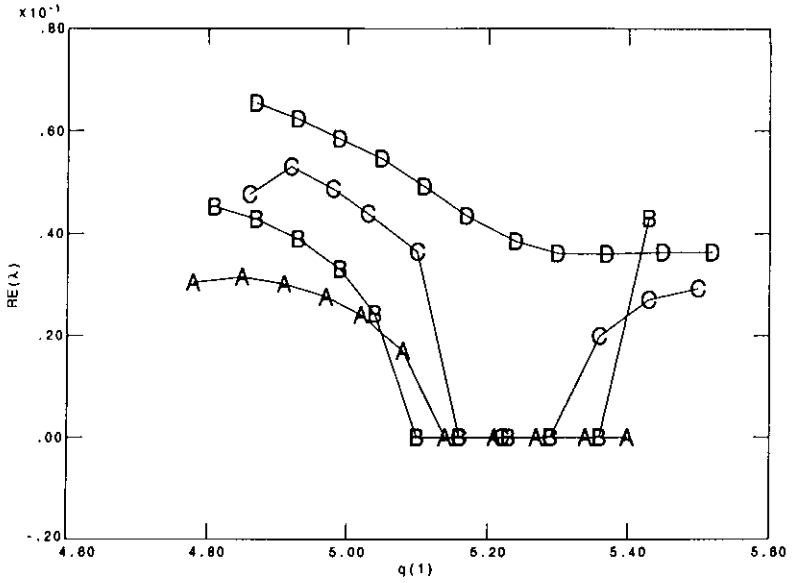

Figure 14: The growth rate of the $n = -1$ ideal external kink as a function of q_1, i.e. q at the plasma boundary, for the four 'reference equilibria' (the labels on the curves refer to the equilibrium), where q_1 was varied by changing the triangularity from 0.6 to 0.7.

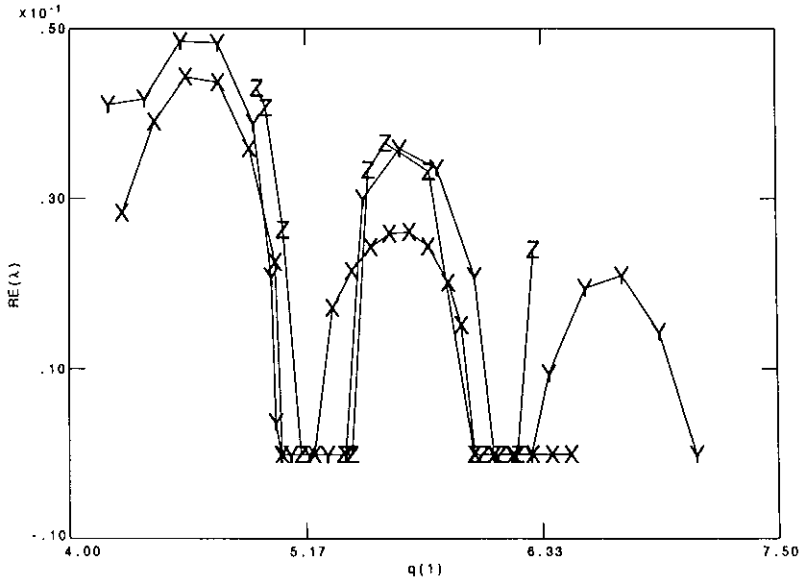

Figure 15: The normalized growth rate for equilibrium B of the $n = -1$ ideal external kink as a function of q_1, where q_1 was varied by changing the total current I_p. Labels X, Y, Z indicate the value for the triangularity, i.e. $\tau = 0.5$, $\tau = 0.6$ and $\tau = 0.7$ respectively.

Equilibrium B					
τ	$\beta(\%)$	g_N	q_0	q_1	**growth rate**
0.7	2.20	2.62	1.22	5.43	4.30×10^{-2}
0.6	2.14	2.56	1.27	4.81	4.54×10^{-2}
0.5	2.09	2.50	1.33	4.36	3.96×10^{-2}
0.4	2.05	2.44	1.39	4.02	4.17×10^{-2}
0.3	2.01	2.40	1.45	3.76	7.00×10^{-2}
b/a	$\beta(\%)$	g_N	q_0	q_1	**growth rate**
1.9	1.99	2.37	1.36	5.38	2.00×10^{-2}
1.8	2.14	2.56	1.27	4.81	4.54×10^{-2}
1.7	2.31	2.76	1.19	4.31	3.53×10^{-2}
1.6	2.50	2.99	1.10	3.85	7.62×10^{-2}
1.5	2.72	3.25	1.02	3.44	10.2×10^{-2}
$\epsilon = a/R_0$	$\beta(\%)$	g_N	q_0	q_1	**growth rate**
0.1500	2.56	3.05	1.07	3.94	7.68×10^{-2}
0.1600	2.39	2.86	1.14	4.24	3.57×10^{-2}
0.1700	2.25	2.68	1.21	4.55	4.88×10^{-2}
0.1786	2.14	2.56	1.27	4.81	4.54×10^{-2}
0.1900	2.01	2.40	1.35	5.18	5.93×10^{-2}
0.2000	1.91	2.27	1.42	5.50	2.87×10^{-2}

Table 8: The effect of the plasma shape parameters on the growth rate of the $n = -1$ ideal external kink for reference equilibrium B. The growth rate is normalized to the Alfvén transit time.

of the reference equilibria. Table 10 illustrates the latter for equilibrium B with a scan of the ellipticity from $b/a = 1.8$ to $b/a = 1.9$. For an ellipticity of 1.85 with $q_1 = 5.09$, we get a stable equilibrium where $\beta = 2.06\%$ and $g_N = 2.46$.

The same ellipticity scans were done for the other reference equilibria and are presented in Figure 16. The figure shows that the reference equilibria C and D can not be stabilized.

The effect of total current was calculated for different ellipticities. Figure 17 compares the reference value of $b/a = 1.8$ with $b/a = 1.7$ and $b/a = 1.9$ for equilibrium B. The 'window of stability' at $q_1 > 5$ and $q_1 > 6$ is the most wide for $b/a = 1.9$.

Aspect ratio

At first sight, it appears difficult to stabilize the kink by changing the value of the inverse aspect ratio $\epsilon = a/R_0$. The inverse aspect ratio scan presented in Table 8 shows that no stabilization is obtained for equilibrium B at an inverse aspect ratio $\epsilon = a/R_0 = 0.19$,

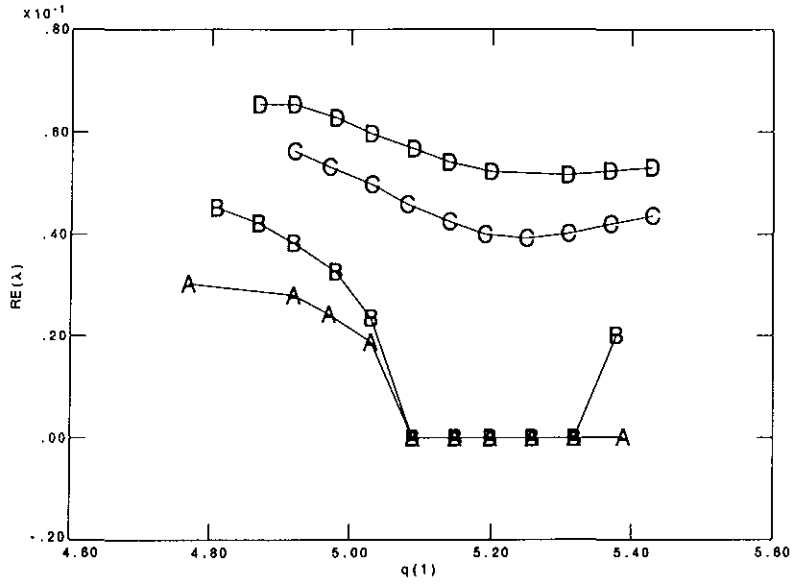

Figure 16: The normalized growth rate of the $n = -1$ ideal external kink as a function of q_1, i.e. q at the plasma boundary, for the four 'reference equilibria' (the labels on the curves refer to the equilibrium), where q_1 was varied by changing the ellipticity from 1.8 to 1.9.

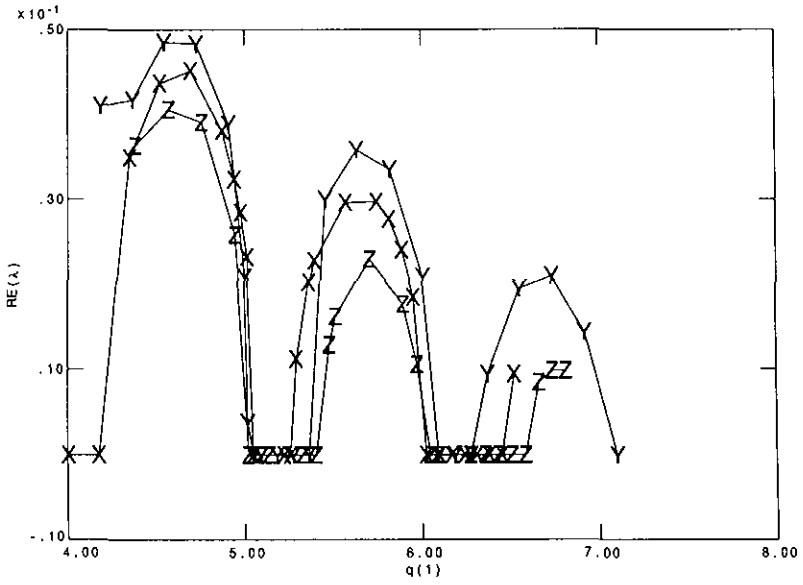

Figure 17: The growth rate for equilibrium B of the $n = -1$ ideal external kink as a function of q_1, where q_1 was varied by changing the total current I_p. Labels X, Y, Z indicate the value for the ellipticity, i.e. $b/a = 1.7$, $b/a = 1.8$ and $b/a = 1.9$ respectively.

Equilibrium B					
τ	$\beta(\%)$	g_N	q_0	q_1	**growth rate**
0.70	2.20	2.62	1.22	5.43	4.30×10^{-2}
0.69	2.19	2.61	1.23	5.36	stable
0.68	2.18	2.60	1.23	5.29	stable
0.67	2.18	2.60	1.24	5.23	stable
0.66	2.17	2.59	1.24	5.16	stable
0.65	2.17	2.58	1.25	5.10	stable
0.64	2.16	2.57	1.25	5.04	2.43×10^{-2}
0.63	2.15	2.57	1.26	4.99	3.31×10^{-2}
0.62	2.15	2.56	1.26	4.93	3.90×10^{-2}
0.61	2.15	2.56	1.27	4.87	4.28×10^{-2}
0.60	2.14	2.56	1.27	4.81	4.54×10^{-2}

Table 9: Detailed calculation of the effect of the triangularity on the growth rate of the $n = -1$ ideal external kink for reference equilibrium B. The growth rate is normalized to the Alfvén transit time.

although $q_1 = 5.18$ (a value for which stabilization might be expected).

The effect of total current was calculated for different values of the inverse aspect ratio. Figure 18 compares the reference value of $\epsilon = 0.1786$ with $\epsilon = 0.17$ and $\epsilon = 0.19$ for equilibrium B. It is remarkable that the external kink in this equilibrium B can not be stabilized for $\epsilon = 0.19$. The 'stability window' at $q_1 > 6$ is wider for $\epsilon = 0.17$. Some analogy can be found with the calculations of the ballooning stability, where a higher β_{max} is found for ϵ below the reference value ($\epsilon = 0.1786, \epsilon^{-1} = 5.6$).

Equilibrium B					
b/a	$\beta(\%)$	g_N	q_0	q_1	**growth rate**
1.90	1.99	2.37	1.36	5.38	2.00×10^{-2}
1.89	2.00	2.39	1.35	5.32	stable
1.88	2.03	2.40	1.34	5.26	stable
1.87	2.04	2.42	1.34	5.20	stable
1.86	2.05	2.44	1.33	5.15	stable
1.85	2.06	2.46	1.32	5.09	stable
1.84	2.08	2.48	1.31	5.03	2.34×10^{-2}
1.83	2.09	2.50	1.30	4.98	3.28×10^{-2}
1.82	2.11	2.52	1.29	4.92	3.84×10^{-2}
1.81	2.12	2.54	1.28	4.87	4.23×10^{-2}
1.80	2.14	2.56	1.27	4.81	4.54×10^{-2}

Table 10: Detailed calculation of the effect of the ellipticity on the growth rate of the $n = -1$ ideal external kink for reference equilibrium B. The growth rate is normalized to the Alfvén transit time.

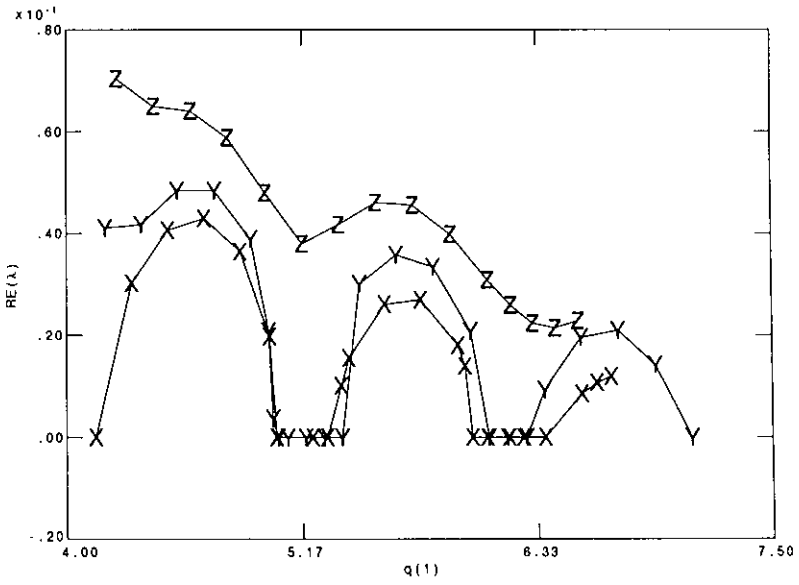

Figure 18: The normalized growth rate for equilibrium B of the $n = -1$ ideal external kink as a function of q_1, where q_1 was varied by changing the total current I_p. Labels X, Y, Z indicate the value for the inverse aspect ratio, i.e. $\epsilon = 0.17$, $\epsilon = 0.1786$ and $\epsilon = 0.19$ respectively.

4.3 Ideal internal kink instabilities

Ideal and resistive internal kink instabilities have been found for equilibria with $q_0 < 1$. An example is shown in Fig. 19 and Table 13. In Fig. 19 the growth rate of the ideal internal kink mode is plotted versus the value of the safety factor at the magnetic axis, q_0. The equilibrium is characterized by $E = b/a = 1.8$, $\tau = 0.6$, $\epsilon = 0.17857$ ($\epsilon^{-1} = 5.6$), and $\bar{I} = 0.754$. With the input profiles $\Gamma(\bar{\psi}) = 1 - \bar{\psi}$ and $\Pi(\bar{\psi}) = 1 - \bar{\psi}$ and the HELENA input parameter B equal to unity this yields $\beta_p = 2.624$ and $\beta = 2.196\%$ ($g = 3.660$, $g_N = 2.913$). The value of the safety factor is 0.767 and has been rescaled for the present calculations which means that the total plasma current is rescaled (see Sect. 4.2).

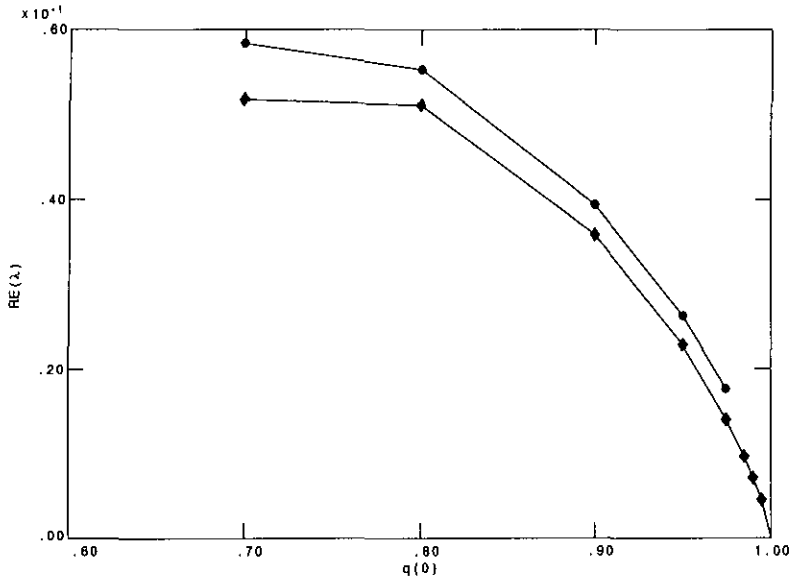

Figure 19: The normalized growth rate of an ideal (diamonds) and resistive (bullets) internal kink instability as a function of q_0.

The ideal internal kink instabilities were calculated with 201 radial grid points and 9 Fourier harmonics, viz. $m = 0, 1, \ldots, 8$. The normalized growth rates vary from 5×10^{-2} for $q_0 = 0.80$, to 3.5×10^{-2} for $q_0 = 0.90$, and 5×10^{-3} for $q_0 = 0.995$ (see Table 13). For $q_0 > 1$ the internal kink modes are stabilized. For the four reference equilibria we found no ideal internal kink instabilities. Fig. 19 and Table 13 also show results on resistive internal kink mode calculations. These will be discussed below in Sect. 5.2.

5 Monotonic q-profiles - non-ideal MHD instabilities

5.1 Resistive external kink instabilities

The resistive MHD spectrum exhibits additional instabilities. Resistive external kink instabilities have characteristics similar to the characteristics of ideal external kink modes. An equilibrium comparable to reference equilibrium A was studied. Table 11 displays the dependence of the growth rate on the position of the perfectly conducting wall surrounding the plasma. The wall has a clear stabilizing effect on the resistive external kink modes.

R_{wall}							
10.0	2.0	1.8	1.6	1.4	1.2	1.15	1.1
5.98	5.59	5.34	4.85	3.85	1.91	1.17	stable

Table 11: The effect of the wall position R_{wall} (normalized to the small radius a) on the growth rate of the $n = -1$ resistive external kink. The figures $\times 10^{-2}$ represent the growth rate (normalized to the Alfvén transit time) at different wall positions for a normalized $\eta = 10^{-5}$, $NG = 50$, $M = 14$.

The growth rates displayed in Table 11 can be compared to the growth rates of the ideal external kink modes found for reference equilibrium A and displayed in Table 6. The growth rates of the resistive external kink modes are higher. ALso, the wall needs to be shifted closer to the plasma surface to get stabilitzation for the resistive external kink modes. Below, we discuss the convergence of the growth rate with respect to the number of radial grid points NG, the number of Fourier components M (two numerical parameters) and the normalized plasma resistivity η:

$$\eta = \frac{\eta^*}{\mu_0 R_0 V_A}, \tag{15}$$

with V_A the Alfvén velocity, $V_A = B_0/\mu_0\rho_0$ (see [3]).

5.1.1 Convergence studies

Table 12 shows that a good estimation of the growth rate is already attained for $NG = 10$. The figure for the growth rate is more sensitive to the number of Fourier components M. From Table 12 it is clear that with 12 or less poloidal Fourier harmonics CASTOR converges but the obtained growth rate is much lower than the converged one. With 16 or more Fourier modes one gets a 'reasonable' estimate. From Fig. 20 it is clear that the growth rate scales roughly with M^{-2} as expected with CASTOR.

5.1.2 Effect of the plasma resistivity

The growth rate is very sensitive to the value for η. Calculations show a $\eta^{1/2}$ scaling with growth rates from 1.14×10^{-1} for $\eta = 10^{-4}$ to 2.63×10^{-3} for $\eta = 10^{-7}$. At realistic

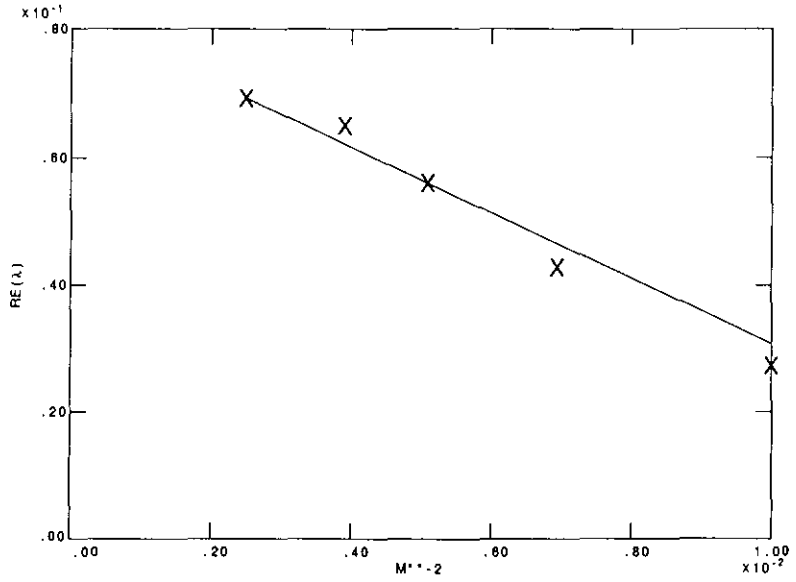

Figure 20: Convergence study of the growth rate of the resistive external kink versus the number of poloidal Fourier harmonics.

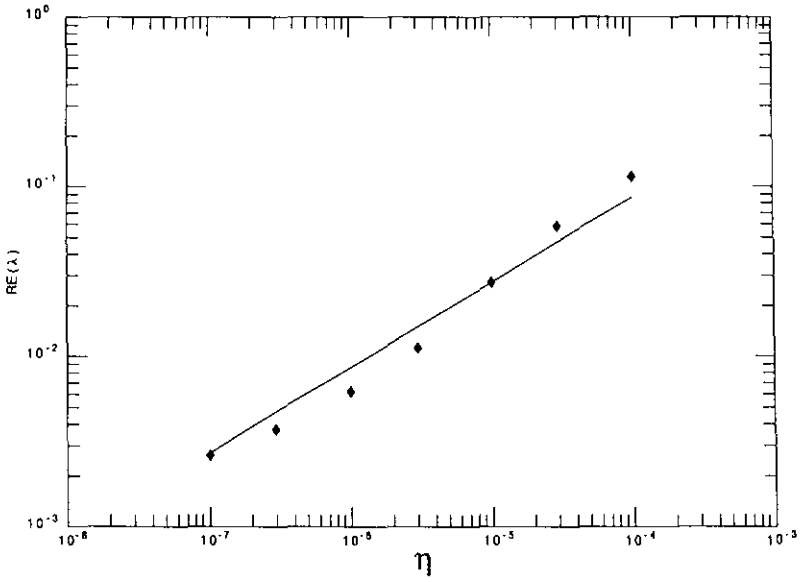

Figure 21: The growth rate of the resistive external kink as a function of η.

	NG						
	5	10	25	50	100	150	201
M = 10			2.894	2.988	2.898	2.899	2.899
M = 12	4.159	4.532	4.543	4.552	4.553	4.554	4.554
M = 14			5.963	5.978	5.980	5.987	5.984
M = 16			6.928	6.947	6.950	6.949	
M = 20			7.486	7.501	7.504		

Table 12: The growth rate $\times 10^2$ (normalized to the Alfvén transit time) of the $n = -1$ resistive external kink as a function of the number of radial gridpoints NG and the number of Fourier harmonics M for $\eta = 10^{-5}$ and $R_{wall} = 2.0$.

tokamak values for η, i.e. $10^{-7} - 10^{-8}$, the resistive external kink modes have growth rates of the order 10^{-3}.

5.2 Resistive internal kink instabilities

Resistive internal kink instabilities have been calculated with 201 radial grid points and 9 Fourier harmonics, viz. $m = 0, 1, \ldots, 8$ (except for $q_0 > 0.985$, these growth rates have been calculated with 15 Fourier modes). The dimensionless electrical resistivity has been set to 10^{-6}. Fig. 19 displays the growth rates of both the ideal and the resistive internal kink instability for the equilibrium described in Sect. 4.3, i.e. the same equilibrium as for which the ideal internal kink instabilities have been calculated. The growth rates of the resistive internal kink instability are somewhat larger than those of the ideal internal kink instability. The difference between the ideal and resistive growth rates is larger for smaller values of q_0. For $q_0 > 0.985$ we increased the number of poloidal Fourier modes to 15 and tried mesh accumulation at the plasma edge. However, no convergence has been obtained for the resistive internal kink modes for $q_0 > 0.985$.

5.3 MARFEs, thermal MHD instabilities

Beside the β-limit, other operational limits of tokamaks can be encountered. A spectacular border observed during the operation of tokamak machines is the density limit. A plasma collapse is observed at the density where the radiative power loss, which increases with density, exceeds the input power. This phenomenon is observed in all tokamaks for mean densities $\bar{n}$ above some threshold density, which increases linearly with the plasma current I_p [11]. The density limit is characterized by a value of ρ in the range of $0.5 < \rho < 1.0$ where

$$\rho \equiv \frac{\bar{n}(10^{20}\mathrm{m}^{-3})}{I_p(\mathrm{MA})/\pi ab(\mathrm{m}^2)}. \tag{16}$$

Close to the density limit, at values for ρ between 0.4 and 0.7, an instability can become active, the MARFE. The MARFE, a precursor to disruption, is a cold but dense plasma condensation, toroidally symmetric, localized at the plasma edge on the inside of the plasma cross section. It is attributed to a radiative thermal instability: a local decrease

q_0	$\eta = 0$	$\eta = 10^{-6}$
0.700	5.180×10^{-2}	5.840×10^{-2}
0.800	5.114×10^{-2}	5.532×10^{-2}
0.900	3.590×10^{-2}	3.939×10^{-2}
0.950	2.292×10^{-2}	2.641×10^{-2}
0.975	1.412×10^{-2}	1.773×10^{-2}
0.985	0.973×10^{-2}	1.350×10^{-2}
0.990	0.758×10^{-2}	no convergence
0.995	0.480×10^{-2}	no convergence
1.000	0.0	no convergence

Table 13: The growth rates of an ideal and resistive internal kink instability for different values of q_0.

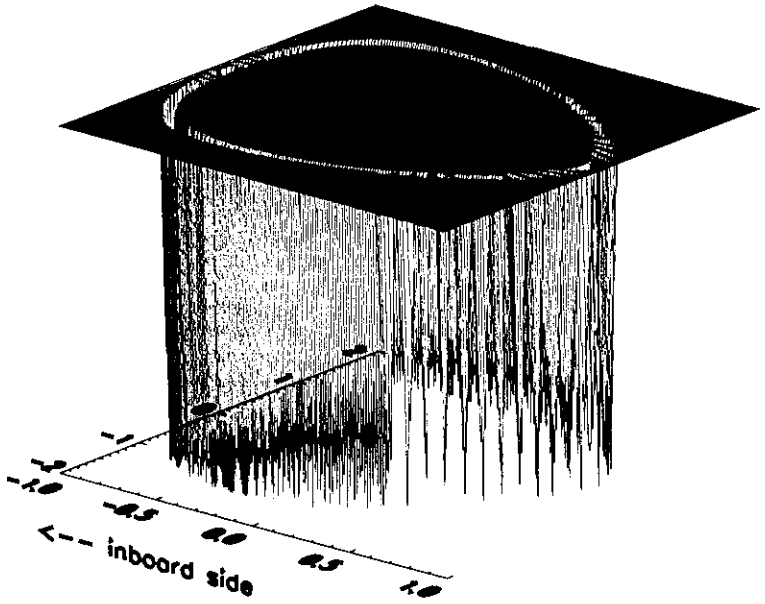

Figure 22: The temperature perturbation by a thermal instability.

of temperature enforces the impurity radiation, so that the temperature decreases even further. This instability will develop fully, unless thermal conduction is able to compensate

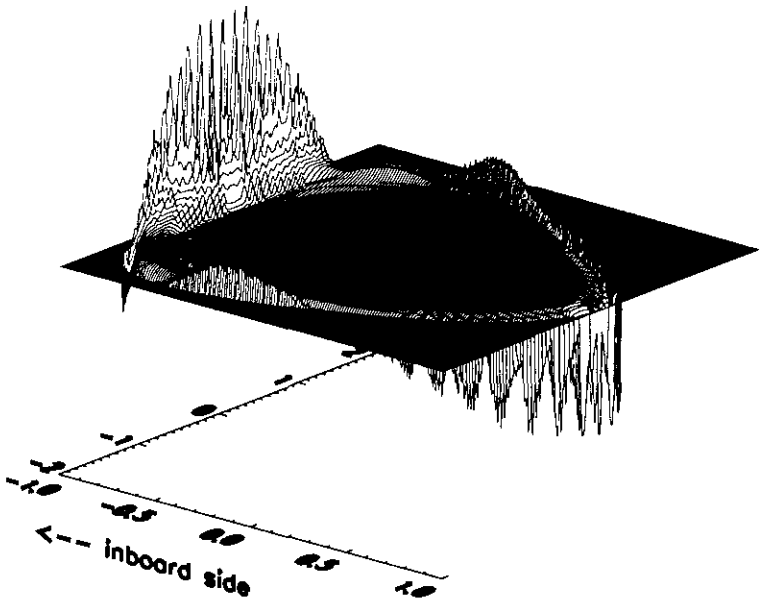

Figure 23: The density perturbation by a thermal instability.

this heat loss.

An extension of CASTOR has been made to study this thermal instability [12]. This extension of CASTOR includes the effects of radiation and heat conduction in the MHD model. Starting from a JET equilibrium where MARFEs occurred, we made a typical 'MARFE equilibrium' for the KT2 tokamak : $I_p = 500\,\mathrm{kA}$, $a = 0.25\,\mathrm{m}$, the ellipticity $b/a = 1.8$, a central density $n_c = 6.0 \times 10^{19}\,\mathrm{m}^{-3}$ yielding a value for $\rho \approx 4.2$, a broad density profile with large gradient at the edge, $\tau = 0.6$, $\epsilon = 0.1786$, $B_t = 3\,\mathrm{T}$, and central temperature $T_c = 2\,\mathrm{keV}$. This equilibrium describes a low β ($\beta = 0.13\%$, $\beta_p = 1.24$, $g_N = 0.15$), but high density plasma. Calculations on this equilibrium indeed yield thermal instabilities with characteristic growth rates of milliseconds. The fastest growing mode has a normalized growth rate of 9.33×10^{-5}. The eigenfunctions have a characteristic behaviour with a poloidally symmetric lowering of the temperature (see Fig. 22), a density increase at the inside of the tokamak (see Fig. 23), and massa flow from the outside to the inside (see Fig. 24).

These calculations illustrate that, similar to all other tokamaks, MARFEs and density limit disruptions can be expected in the KT2 tokamak at high densities.

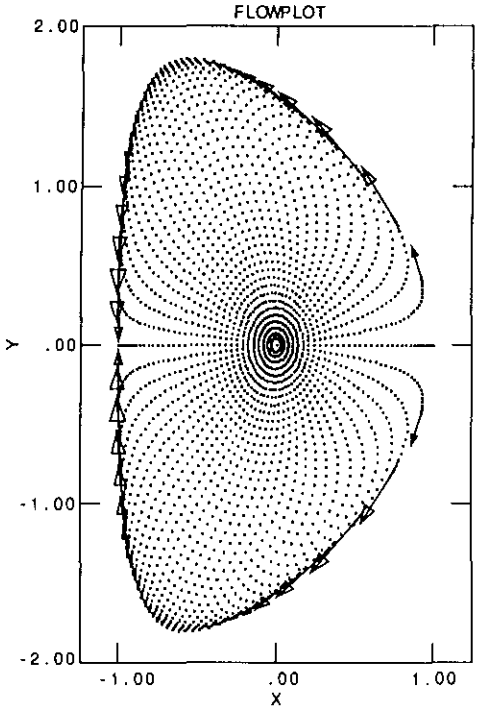

Figure 24: The velocity perturbation by a thermal instability in a cross section of the tokamak.

6 Inverted safety factor profiles - ideal MHD instabilities

For the study of 'advanced tokamak scenarios' for KT-2 the total current is lowered to $\bar{I} = 0.754$ corresponding to $B = 2\,\mathrm{T}$ and $I_p = 300\,\mathrm{kA}$.

6.1 Ballooning stability

In the present section, a profile optimization study for the KT-2 advanced tokamak scenario is presented. The current density profile is fixed to a typical average current density profile produced by the transport code JETTO in the modelling phase of the profile control experiments at JET yielding a fixed inverted q-profile. The pressure profile is then optimized in order to increase the plasma beta as far as possible. In the present subsection, the pressure profile is optimized with respect to ballooning instabilities. The external kink instabilities and the infernal modes for the resulting 'marginally ballooning stable' profiles are investigated in the next subsection. Below, we first describe the equilibrium profiles used as a starting point for the optimization study. Next, the optimization procedure itself is described because it involves a slight modification of the 'standard' profile optimization procedure used for monotonic q-profiles. Finally, the 'marginally ballooning stable' pressure profile is discussed in some detail.

6.1.1 Reference equilibrium

There is a lot of freedom in the choice of the input profiles $\Gamma(\bar{\psi})$ and $\Pi(\bar{\psi})$ yielding an inverted q-profile. As reference profiles we take the typical average current density profile and pressure profile as produced by the transport code JETTO in the modelling phase of the profile control experiments at JET. This current density profile and pressure profile have also been used as reference profiles in an MHD stability analysis of advanced tokamak scenarios at JET [13]. Together with KT-2 specifications $\epsilon^{-1} = 5.6$, $\bar{I} = 0.754$ ($B = 2\,\mathrm{T}$ and $I_p = 300\,\mathrm{kA}$), $b/a = 1.8$, and $\tau = 0.6$, they yield the profiles displayed in Fig. 25.

This reference equilibrium has a poloidal beta of 2.931 and a toroidal beta of 2.454% which corresponds to the normalized beta (Troyon factor) $g_N = 3.255$ ($g = 4.090$). The pressure gradient is largest halfway between the magnetic axis and the plasma edge, i.e. very close to the region of small negative shear. The safety factor at the edge is high: $q_1 = 6.46$. At the magnetic axis $q_0 = 2.02$, while the safety factor reaches its minimum at $\bar{\psi} = .42$ where $q_{\min} = 1.64$.

6.1.2 Local optimization procedure

Below we will specify a relevant current density profile and look for the optimal pressure profile that corresponds to it. Here 'optimal' means 'marginal ballooning stable'. If the marginal ballooning stable pressure profile is increased locally, e.g. at one specific $\bar{\psi}$-value, that magnetic surface becomes immediately ballooning unstable. Also, when the plasma beta is increased, e.g. by increasing the horizontal shift of the magnetic axis, all magnetic surfaces become ballooning unstable at once.

The 'standard' local optimization procedure of the pressure profile for a fixed average current density profile consists of the following steps:

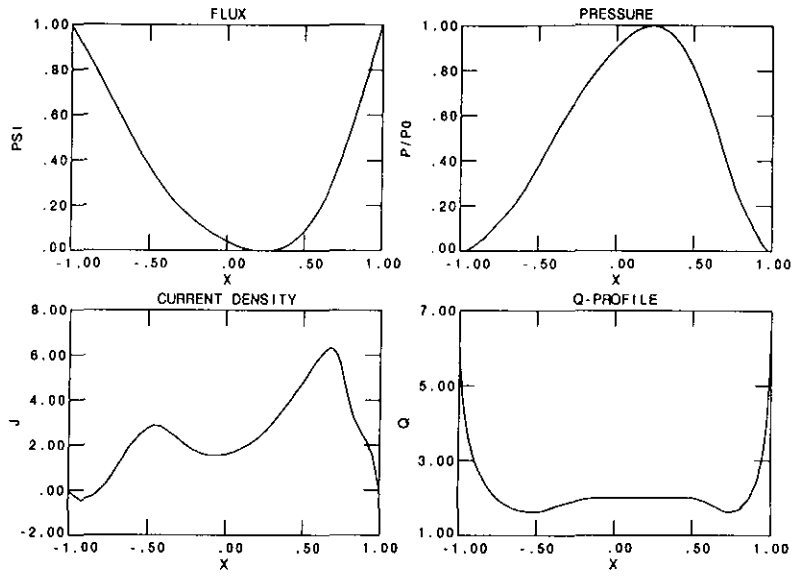

Figure 25: The $\bar{\psi}$, $\bar{P}(\bar{\psi})$, $J_\phi(\bar{\psi})$, and $q(\bar{\psi})$-profile for the 'reference' equilibrium used as starting point for the pressure profile optimization procedure. This equilibrium has $\epsilon = 0.17857$ ($\epsilon^{-1} = 5.6$) and $\bar{I} = 0.754$ ($B = 2\,\mathrm{T}$ and $I_p = 300\,\mathrm{kA}$). The shape of the poloidal cross-section is characterized by $b/a = 1.8$ and $\tau = 0.6$.

step 1: choose the current density profile and keep it fixed (on average) such that the q-profile is almost fixed;

step 2: specify a Π-profile on a discrete $\bar{\psi}$-grid (e.g. 10 grid points);

step 3: increase the value of the parameter δ, i.e. the shift of the magnetic axis;

step 4: adjust the Π-profile locally, starting at the innermost ballooning unstable point, i.e. decrease the input value of Π at the lowest $\bar{\psi}$-value where a ballooning instability occurs until that magnetic surface is ballooning stable, then go to step 3 and repeat until marginal stability is obtained.

This procedure is frequently used to find 'marginal ballooning stable' pressure profiles for standard tokamak equilibria with monotonic q-profiles.

However, the 'standard' local optimization procedure described above does not work satisfactorily for 'advanced' tokamak equilibria with inverted safety factor profiles. We tried it on the reference equilibrium described in the previous section and it works well up to the point where the horizontal shift of the magnetic axis becomes larger than 0.30. At that point HBT can not handle the extreme equilibrium conditions any more and the iteration procedure does not converge any more. Therefore, we have applied a slightly different optimization procedure which has also been used in previous optimization studies for advanced tokamak scenarios at JET [13]. This local optimization procedure for the pressure profile consists of the following steps:

step 1: choose the current density profile and keep it fixed (on average) such that the q-profile is almost fixed;

step 2: specify a Π-profile on a discrete $\bar{\psi}$-grid (e.g. 10 grid points);

step 3: choose a value of the parameter δ that yields ballooning instability from $q_{\min}$ on to some other $\bar{\psi}$-value;

step 4: keep the parameter δ fixed and decrease the Π-profile locally, starting at the innermost ballooning unstable point, until all flux surfaces are ballooning stable;

step 5: now increase the Π-profile locally, starting from the innermost flux surface that was stable in step 3 (stop just before a ballooning instability occurs);

step 6: iterate a few times on step 5, i.e. increase the Π-profile locally working from $q_{\min}$ on outwards (stop just before a ballooning instability occurs).

6.1.3 Optimization results

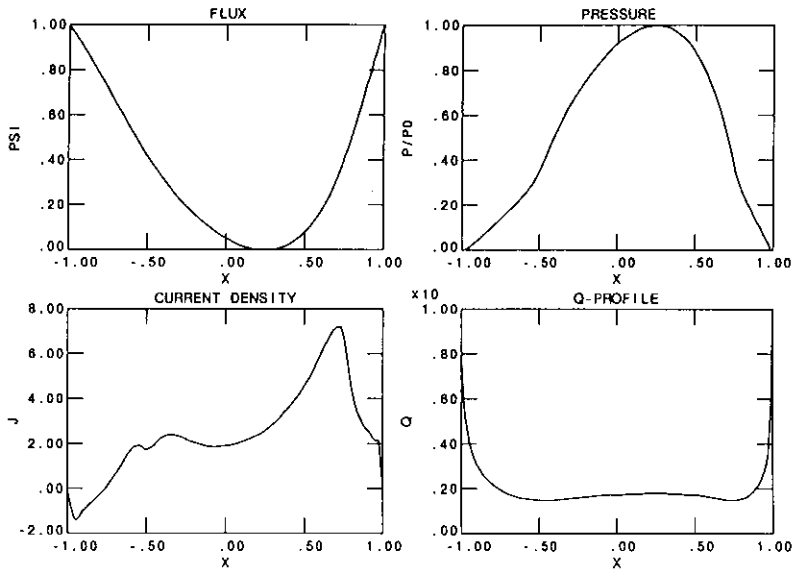

Figure 26: The $\bar{\psi}$, $\bar{P}(\bar{\psi})$, $J_\phi(\bar{\psi})$, and $q(\bar{\psi})$-profile for the 'optimal' equilibrium with a marginally stable pressure profile.

The pressure profile of the reference equilibrium described in Sect. 6.1.1 has been optimized with the local optimization procedure described in the previous section. The position of the magnetic axis is given by $\delta = 0.25$. The $\Pi(\bar{\psi})$-profile has been discretized in 21 grid points, equidistant in $\bar{\psi}$. For $\bar{\psi} \leq 0.425$ the value of $\Pi(\bar{\psi})$ has been put equal to unity.

The equilibrium is then only ballooning unstable in $\bar{\psi} = 0.45$. After three iteration steps of the procedure described in the previous section, the marginally stable pressure profile is obtained. The new equilibrium profiles are displayed in Fig. 26. The pressure profile is marginally ballooning stable in the sense that increasing the input $\Pi(\bar{\psi})$-profile locally by as little as 0.01 yields a ballooning instability at that magnetic surface ($0.45 \leq$

M	**growth rate**
15	2.848×10^{-2}
17	7.287×10^{-2}
19	1.094×10^{-1}
21	1.164×10^{-1}
23	1.281×10^{-1}
25	1.350×10^{-1}

Table 14: Convergence study of the growth rate of the instability versus the number of poloidal Fourier harmonics with CASTOR.

$\bar{\psi} \leq 0.95$). Moreover, increasing the value of δ, i.e. the shift of the magnetic axis, to 0.26 makes all magnetic surfaces from $\bar{\psi} = 0.45$ to $\bar{\psi} = 0.95$ ballooning unstable at once!

The marginally stable equilibrium obtained with the local optimization procedure as described above has a plasma beta of 3.425% and $\beta_p = 4.086$. This corresponds to quite high Troyon factors, viz. $g_N = 4.540$ and $g = 5.705$.

We increased the horizontal shift of the magnetic axis by 10% to $\delta = 0.275$ and repeated the whole optimization procedure. After three iterations the marginal ballooning stable pressure profile is obtained again. The equilibrium profiles are very similar to the ones displayed in Fig. 26. The plasma beta, however, is slightly higher, viz. $\beta_p = 4.230$ and $\beta = 3.542\%$ ($g_N = 4.697$ and $g = 5.902$).

6.2 External kink instabilities and/or infernal modes

In JET, plasmas with a non-monotonic q-profile and negative shear in the plasma centre have been obtained with pellet injection [14]. This resulted in improved confinement. However, this phase turned out to be transient and it usually ended with an MHD instability which led to a redistrubution of the current and a monotonic q-profile. It has been suggested that 'infernal modes' are the most likely condidate for the observed instability [15]. Infernal modes are driven by a large pressure gradient in the region of low shear near the minimum in the q-profile. We have looked for infernal modes for the marginally ballooning stable equilibria discussed above. One problem with infernal modes is that they require a high spatial resolution. In particular the number of Fourier modes is typically quite high. Hence, we first did a convergence study for the number of Fourier modes with CASTOR. The results are presented in the next section. The effect of the triangularity of the cross-section of the equilibrium plasma on the instability is discussed in Sect. 6.2.2. The instability we found turns out to be an external mode. This is exemplified by shifting the wall towards the plasma surface which results in a decrease of the growth rate of the instability as shown in Sect. 6.2.3. Finally, we discuss the effect of changing the plasma resistivity on this external instability in Sect. 6.2.4.

6.2.1 Convergence study

For the convergence study of the instability growth rate with respect to the number of Fourier modes we considered the marginally ballooning stable equilibrium with $\beta_p = 4.230$ and $\beta = 3.542\%$ ($g_N = 4.697$ and $g = 5.902$) discussed in Sect. 6.1.3. However, we considered a triangularity $\tau = 0.4$ for reasons that will become clear in the next section. The safety factor is then 2.063 at the magnetic axis and decreases to 1.686 at $\bar{\psi} = 0.374$. Then, the safety factor increases again to 5.773 at the plasma edge. For the convergence study the equilibrium has been rescaled with $q_0 = 2.55$. The wall is placed at 2.0 and the plasma resistivity is set equal to zero. We used 101 radial grid points. The results are displayed in Table 14 and Fig. 27.

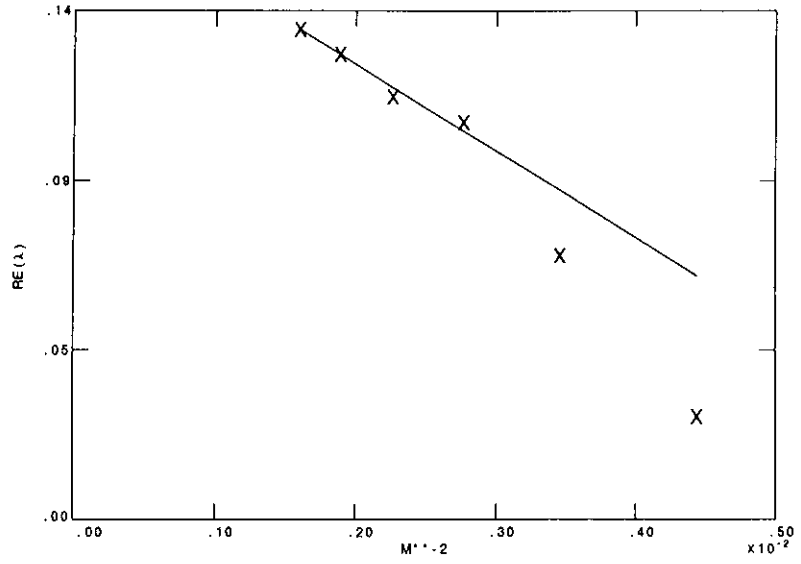

Figure 27: Convergence study of the growth rate of the instability versus the number of poloidal Fourier harmonics.

From Table 14 it is clear that with 15 or less poloidal Fourier harmonics CASTOR converges but the obtained growth rate is much lower than the converged one. With 21 or more Fourier modes one gets a 'reasonable' estimate. From Fig. 27 it is clear that for $M > 17$ the growth rate scales, as M^{-2} as expected with CASTOR.

6.2.2 Effect of the triangularity of the cross-section

The convergence study presented in the previous subsection showed that a lot of poloidal Fourier harmonics are required to get a good estimate of the growth rate of the instability in the case of the optimized ballooning stable equilibrium. For lower values of the triangularity of the cross-section, however, less Fourier modes are required to get a reasonable estimate of the growth rate. In order to study the effect of the triangularity on the instability growth rate we made q_0-scans of the growth rate for different values of the triangularity τ. The results are displayed in Fig. 28. These results are obtained with 101

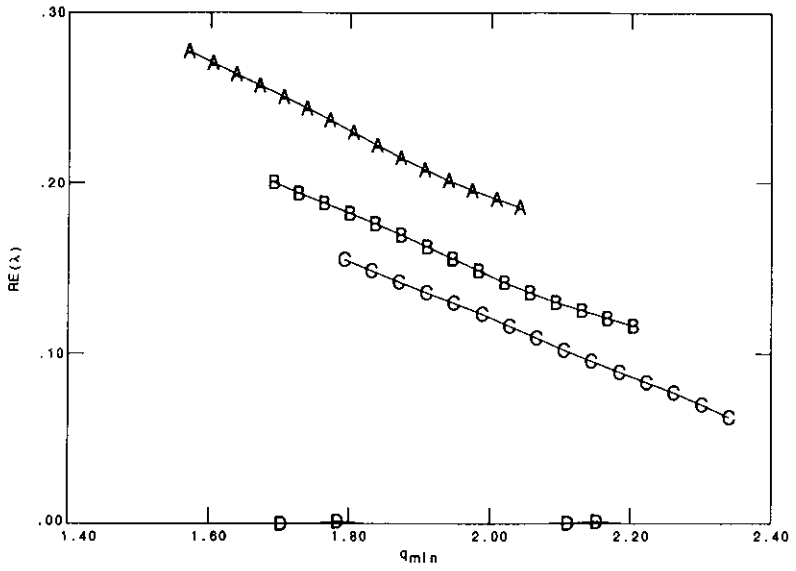

Figure 28: Growth rate versus $q_{\min}$ for a marginal ballooning stable equilibrium and for different triangularities: A) $\tau = 0$ ($M = 15$), B) $\tau = 0.2$ ($M = 15$), C) $\tau = 0.4$ ($M = 19$), and D) $\tau = 0.6$ ($M = 23$).

radial grid points and 15 Fourier harmonics for $\tau = 0$ and $\tau = 0.2$. For $\tau = 0.4$ we used 19 poloidal Fourier harmonics and for $\tau = 0.6$ we used 23 harmonics.

In Fig. 28 the growth rate is plotted versus $q_{\min}$ because the $n = -1$ infernal mode is known to stabilize at $q_{\min} = 2$, i.e. when there is no $q = 2$ magnetic surface inside the plasma [13]. However, as seen in Fig. 28 the mode does not stabilize at $q_{\min} = 2$. Hence, the mode has clearly a different character than the 'infernal' modes found in JET stability studies. As a matter of fact, the flow plot displayed in Fig. 29 reveals that the modes we found here are external modes with a large internal component. The amplitude of the velocity field is largest near the plasma edge. Also, below we will show that the mode stabilizes as the wall is shifted towards the plasma surface which is not the case for the 'infernal' modes found in the JET stability analysis.

From Fig. 28 it is also clear that the increase of the triangularity of the poloidal cross-section of the plasma has a stabilizing effect on this external mode. As a matter of fact, the growth rates of the instability decrease as τ increases. For $\tau = 0.6$ the growth rates are considerably smaller. The results for $\tau = 0.6$ have been obtained with 23 Fourier modes and for these high values of τ an even higher spatial resolution would be preferable. However, for such high spatial resolutions CASTOR requires a lot of computer memory and CPU time. It is the latter requirement that yields the restriction. As a matter of fact, it already took about 8 CPU hours on a Cray C98 to produce the $q_{\min}$-scan for $\tau = 0.6$ in Fig. 28.

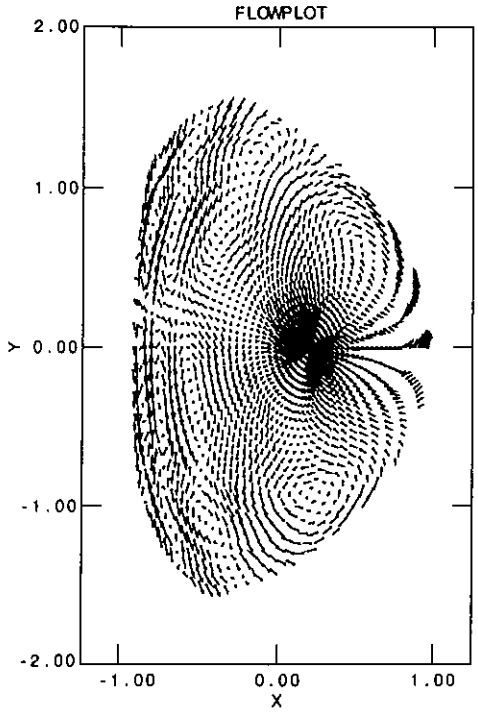

Figure 29: Flow plot of the instability found for $\tau = 0.4$ and $R_{wall} = 2$.

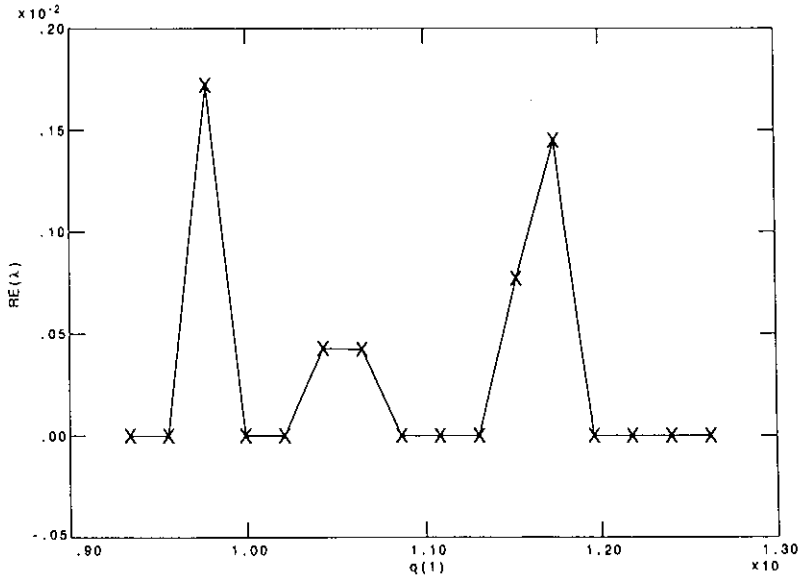

Figure 30: Growth rate versus q_1 for a marginal ballooning stable equilibrium and for $\tau = 0.6$ ($M = 23$).

Fig. 30 shows the same $\tau = 0.6$ growth rates as in Fig. 28. However, in Fig. 30 the scale on the vertical axis is different and the growth rates are plotted versus the value of the safety factor at the plasma edge rather than versus the minimal value of the safety factor. In Fig. 30 it can be seen that for $\tau = 0.6$ stability windows occur at the location where one would expect them for an external mode, viz. just above integer values of q_1, as discussed above in the sections on external kink modes. Remark that the poor spatial resolution of Fig. 30 is due to the high CPU time costs for these calculations.

Notice that the growth rate of this external instability is much larger than the growth rates of the external kink modes obtained for monotonic safety factor profiles in Sect. 4.2. Yet, the equilibrium studied here has a much larger value of the safety factor at the plasma edge. For higher magnetic shear we could expect lower growth rates. A comparison of Fig. 29 with Fig. 10 shows that the mode we found here is a more global mode which has a more deteriorating effect on the plasma.

6.2.3 Effect of the wall position

The ultimate proof of the statement that the mode discussed in the previous subsection is indeed an external mode can be given by studying the effect of the position of the external wall surrounding the plasma and the vacuum around it. The results of such a study are displayed in Table 15. Shifting the wall towards the plasma surface indeed results in a decrease of the growth rate of the instability. For $R_{wall} = 1.15$ the mode is stabilized. This proves it is indeed an external mode as the instability does not exist in a fixed boundary plasma.

R_{wall}	**growth rate**
2.000	1.350×10^{-1}
1.500	1.031×10^{-1}
1.300	5.827×10^{-2}
1.250	4.164×10^{-2}
1.200	2.278×10^{-2}
1.175	1.137×10^{-2}
1.150	–

Table 15: Effect of the position of the perfectly conducting wall on the growth rate of the instability for $\tau = 0.4$ and $q_0 = 2.55$ ($M = 25$, $NG = 101$).

6.2.4 Effect of the resistivity

Finally, the effect of resistivity on the growth rate of the external mode has been investigated. The resistivity has been varied from 10^{-5} to 10^{-9}. The growth rate of the

η	**growth rate**
0.0000	1.350×10^{-1}
1.0×10^{-9}	1.352×10^{-1}
1.0×10^{-8}	1.358×10^{-1}
1.0×10^{-7}	1.358×10^{-1}
1.0×10^{-6}	1.461×10^{-1}
1.0×10^{-5}	1.778×10^{-1}

Table 16: Effect of the resistivity on the growth rate of the instability for $\tau = 0.4$ and $q_0 = 2.55$ ($M = 25$, $NG = 101$).

instability is not very sensitive to the value for the plasma resistivity η. This is clear from Table 16 where the growth rates of a typical instability are displayed for different values of the resistivity. Changing the plasma resistivity from 10^{-9} to 10^{-5}, i.e. four orders of magnitude, results in an increase of the growth rate of only 31%.

At realistic tokamak values for η, i.e. $10^{-7} - 10^{-8}$, we have growth rates which are almost the same as those found in the ideal MHD, i.e. for $\eta = 0$. This proves that this external mode is in nature an ideal MHD instability.

7 Training of KAERI staff and code transfer

It was agreed to provide support to install the numerical codes on the KAERI computer and to train KAERI staff members in MHD stability analysis by means of HELENA and CASTOR.

7.1 Training of KAERI staff

Dr. B.G. Hong visited from 8 to 14 July 1995. During this visit, the equations, definitions, input parameters and output parameters of the codes HELENA and CASTOR were discussed extensively. Also, a 'HELENA installation and user guide' and a 'CASTOR installation and user guide' have been written [7, 8]. Together with the already existing HBT user guide [4] the information contained in these installation and user guides will facilitate the installation and use of the numerical codes considerably.

7.2 Installation of numerical codes on the KAERI computer

During the visit of Dr. B.G. Hong at Rijnhuizen, the REVISE toolkit has been installed on the Cray computer used by KAERI. REVISE is a portable facility for the systematic maintenance of large computer programs which combines the positive features of updating and screen editing (rigor and speed), while avoiding the negative ones (slowness and generation of errors). The REVISE package was developed to control and exchange the progression of changes, avoiding the introduction of mistakes, informing fellow collaborators in an international group of scientists of new versions of the numerical tools they are all using for different purposes.

The CASTOR code was already available at KAERI but it had not been installed properly. We have installed CASTOR on the Cray computer used by the KAERI staff. Also, HELENA and HBT have been installed on that computer as well as the required subroutine libraries PPPLIB (Plasma Physics Plotting LIBrary) and HGOLIB and some diagnostic programs.

8 Conclusions

The MHD stability of KT-2 tokamak plasmas has been analyzed by means of three computer codes, viz. HBT, to construct the equilibria and to perform the ballooning mode stability analysis, CASTOR, for the study of the low-n MHD instabilities, and HELENA, used as an interface between HBT and CASTOR.

First, the ideal and dissipative MHD stability of KT-2 equilibria with monotonic q-profiles has been investigated. An equilibrium with a plasma current of 500 kA, a magnetic field of 3 Tesla, and a poloidal cross-section with ellipticity $b/a = 1.8$ and triangularity $\tau = 0.6$ was taken as a reference. A δ-optimization procedure for a scan of the input profile $\Gamma(\bar{\psi})$ for four different $\Pi(\bar{\psi})$-profiles yielded four ballooning stable equilibria with monotonic q-profiles. These four equilibria differ in the localization of the pressure profile and the steepness of the current density profile and have been used as 'reference equilibria' for the ballooning stability analysis and for the study of ideal and resistive external kink instabilities.

Varying the ellipticity of the cross-section from 1.2 to 1.9 leads to an increase of roughly 10% of the maximal plasma beta that still yields a ballooning stable equilibrium and an increase of roughly 50% of the poloidal plasma beta. However, the dependence of β_{max} on b/a is not monotonic for all four reference equilibria and $b/a = 1.8$ is the optimum on the whole. A similar scan of the triangularity of the cross-section ($0.2 \leq \tau \leq 0.7$) revealed that $\tau = 0.6$ yields optimal ballooning stability conditions for all four reference equilibria. The value of the parameter β_{max}, the maximal plasma beta yielding a ballooning stable equilibrium, and the value of the corresponding $\beta_{p\,max}$ turned out to scale almost linearly proportional to the aspect ratio. Decreasing the total plasma current from 550 kA to 300 kA results in a monotonic decrease of β_{max} while the marginal beta poloidal increases substantially, viz. by roughly 50

It has been shown that the four equilibria are subject to external kink instabilities when the conducting shell around the plasma is situated far away from the plasma surface. Reference equilibrium D has the strongest current density gradient at the plasma edge and turns out to be the most unstable equilibrium. The external kink modes can be stabilized by shifting the perfectly conducting wall that surrounds the plasma and the vacuum towards the plasma surface. All four equilibria turned out to be stable with respect to external kink modes for $R_{wall} \leq 1.2$. Varying the total current also affects the growth rates of the ideal external kink modes and, hence, the stability of the equilibria. It turned out that the external kink instabilities in all four reference equilibria can be stabilized by lowering the total plasma current because this increases the value of the safety factor at the plasma edge. However, the steeper the gradient in the current density profile the lower the total current needs to be for stabilization of the external kink instability. For the two reference equilibria with the lowest current density gradients, the stabilization of the $n = -1$ external kink mode already occurs at $I_p = 477$ kA. Inclusion of $n = -2$ kink instabilities nqrrows the stability windows somewhat. A decrease of the plasma beta while keeping the total current constant results in a decrease of the magnetic shear and eventually to a stabilization of the external kink modes.

The influence of the geometric parameters b/a, τ, and ϵ on the growth rates of the $n = -1$ external kink modes has also been investigated. Increasing the triangularity slightly in the reference equilibria leads to an increase of the safety factor at the plasma edge. For three of the four reference equilibria this leads to a stabilization of the $n = -1$

external kink when there is a $q = 5$ rational surface inside the plasma. An increase of the ellipticity of the poloidal cross-section has a similar effect on the stability of the external kink modes. By slightly increasing the ellipticity (to 1.85) q_1 becomes larger than 5 and for two of the reference equilibria this results in a stabilization of the kink mode. The value of the safety factor at the plasma edge can also be increased by increasing the inverse aspect ratio. However, this did not lead to stabilization of the external kink mode. A total current scan at $\epsilon^{-1} = 5.6$ revealed that the kink modes can be stabilized by lowering the total current somewhat. The stability window turns out to be the widest for $\tau = 0.6$. Similar total current scans for different ϵ-values showed that lower inverse aspect ratio values yield lower instability growth rates and wider stability windows. Internal kink modes turned out to be difficult to find. The few ideal internal kink modes we found, stabilized for $q_0 \geq 1$ as expected. The highest value of the Troyon factor g_N obtained in the kink stability analysis for monotonic q-profiles is 2.79 ($\beta = 2.34\%$).

Resistive external and internal kink modes have also been found. Resitivity has a destabilizing influence on these kink modes. The growth rates of the external kink modes are roughly proportional to $\eta^{1/2}$. For the relevant, very high, values of the magnetic Reynolds number these resistive external kink modes are stabilized or have very low growth rates of the order of 10^{-3}, i.e. much smaller than the ideal external kink growth rates. The growth rates of the resistive internal kink modes are roughly 10% higher for $\eta = 10^{-6}$ than for $\eta = 0$. It was also shown that in the KT-2 tokamak MARFEs and density limit desruptions can be expected at high densities.

Next, so-called 'advanced tokamak scenarios' were analyzed for the KT-2 plasma. For these studies the total current has been lowered to 300 kA and a magnetic field of 2 T has been considered. The pressure profile has been optimized locally for a given average current density profile. The input average current density profile was taken from similar studies of the stability of advanced tokamak scenarios at JET. A local optimization procedure yielded the marginally ballooning stable pressure profile, i.e. the pressure profile that is marginally ballooning stable at all magnetic flux surfaces with positive shear. The marginal ballooning stable equilibrium has a $\beta_p = 4.230$ and $\beta = 3.542\%$ which corresponds to quite high Troyon factors: $g_N = 4.697$ and $g = 5.902$. For this optimal equilibrium we looked for 'infernal' modes. Instabilities were indeed found but they turned out to correspond to external modes and, hence, they have a different behaviour than the 'infernal' modes found in a similar stability analysis of JET plasmas with inverted safety factor profiles. A convergence study revealed that for this purpose a high spatial resolution is required. In particular, the number of poloidal Fourier harmonics turned out to have to be larger than 21. The instability we found can be stabilized by shifting the wall towards the plasma surface. The triangularity of the cross-section turned out to have a stabilizing effect on the mode and an increase of τ yielded lower growth rates. For $\tau = 0.6$ we even found stability windows in a scan of the total plasma current. The growth rates are unaffected by the plasma resistivity for relevant values of η, which proves this instability is an ideal MHD stabiltiy in nature. The high spatial resolution needed for this kind of calculations imposes a serious restriction since the requirements for computer memory and CPU time become quite demanding for such high resolutions. As a matter of fact, it took more than 300 Cray C98 CPU hours to produce the results discussed here.

Finally, the numerical codes HBT, CASTOR, and HELENA and all non-standard subroutine libraries used by these codes have been installed on the Cray C98 used by KAERI. Installation and user guides have been written for HELENA and CASTOR.

References

[1] Concept definition of KT-2, a large-aspect-ratio divertor tokamak with FWCD, Korea Atomic Energy Research Institute, KAERI/TR-472/94.

[2] F. Troyon, A. Roy, W.A. Cooper, F. Yasseen, and A. Turnbull, *Plasma Physics and Controlled Fusion*, **30**, 1597-1609 (1988), "Beta limit in tokamaks, experimental and computational status".

[3] G. Huijsmans, Ph.D. thesis, Free University Amsterdam, 1991, "External resistive modes in tokamaks".

[4] G.T.A. Huysmans, R.M.O. Galvão, and J.P. Goedbloed, *Rijnhuizen Report 90-194*, 1990, "Documentation of the high beta stability codes HBT and HBTAS at JET".

[5] G.T.A. Huysmans, J.P. Goedbloed, and W. Kerner, *Proc. CP90 Conf. on Comp. Phys. Proc.*, World Scientific Publ. Co., 1991, p. 371, "Isoparametric Bicubic Hermite Elements for Solution of the Grad-Shafranov Equation".

[6] G.T.A. Huysmans, J.P. Goedbloed, and W. Kerner, *Phys.Fluids* **B**, **5**, 1993, p. 1545, "Free boundary resistive modes in tokamaks".

[7] S. Poedts, H.A. Holties, J.P. Goedbloed, *Rijnhuizen Report 96-228*, 1996, "HELENA: Installation and User Guide".

[8] S. Poedts, H.A. Holties, J.P. Goedbloed, *Rijnhuizen Report 96-229*, 1996, "CASTOR: Installation and User Guide".

[9] S. Poedts, W. Kerner, J.P. Goedbloed, B. Keegan, G.T.A. Huysmans, and E. Schwarz, *Plasma Phys. and Contr. Fusion*, **34**, 1992, p. 1397, "Damping of global Alfvén waves in tokamaks due to resonant absorption".

[10] J.P. Goedbloed, *Comp. Phys. Comm.*, **24**, 311-321 (1981), "Conformal mapping methods in two-dimensional magnetohydrodynamics"

[11] B. Lipschultz, *J. Nucl. Mater.*, **145-147**, 15 (1987), "Review of MARFE phenomena in tokamaks".

[12] A. De Ploey, R.A.M. Van der Linden, G.T.A. Huysmans, M. Goossens, W. Kerner, and J.P. Goedbloed, *22nd EPS Conf. on Controlled Fusion and Plasma Physics*, **19C**, Part I, eds. B.E. Keen, P.E. Stott, and J. Winter, Bournemouth, 3 - 7 July 1995, pp. 221–224, "MARFEs: a magnetohydrodynamic stability study of general tokamak equilibria".

[13] H.A. Holties, G.T.A. Huysmans, W. Kerner, J.P. Goedbloed, F.X. Söldner, and V.V. Parail, *21st EPS Conf. on Controlled Fusion and Plasma Physics*, **18B**, Part I, eds. E. Joffrin, P. Platz, and P.E. Stott, Montpellier, 27 June - 1 July 1994, pp. 234–237, "MHD stability of advanced tokamak scenarios".

[14] M. Hugon, B.Ph. van Milligen, P. Smeulders, L.C. Appel, D.V. Bartlett, D. Boucher, A.W. Edwards, L.-G. Eriksson, C.W. Gowers, T.C. Hender, G. Huysmans, J.J. Jacquinot, P. Kupschus, L. Porte, P.H. Rebut, D.F.H. Start, F. Tibone, B.J.D. Tubbing, M.L. Watkins, and W. Zwingmann, *Nuclear Fusion*, **32**, 33 – 43 (1992), "Shear reversal and MHD activity during pellet enhanced performance pulses in JET".

[15] L.A. Charlton, L.R. Baylor, A.W. Edwards, G.W. Hammett, W.A. Houlberg, P. Kupschus, V.E. Lynch, S.L. Milora, J. O'Rourke, and G.L. Schmidt, *Nuclear Fusion*, **31**, 1835 – 1842 (1991), "Theoretical analysis of the role of the infernal mode in the stability of peaked pressure profiles in pellet fuelled JET discharges".